JOURNAL OF PETROLOGY

Journal of Petrology, 2021, Vol. 62, No. 8, 1–29
doi: 10.1093/petrology/egab008
Advance Access Publication Date: 4 February 2021
Original Manuscript

OXFORD

Subcratonic and tectonic evolution of pyroxenite and eclogite with lamellar inclusions in garnet, Western Gneiss Region, Norway

Dirk Spengler,[1,*] Taisia A. Alifirova,[2,3] and Herman L. M. van Roermund[4]

[1]Institut für Mineralogie und Kristallchemie (closed), Universität Stuttgart, Azenbergstraße 18, Stuttgart, 70174, Germany; [2]Sobolev Institute of Geology and Mineralogy, Siberian Branch, Russian Academy of Sciences, 3 Academician Koptyug ave, Novosibirsk, 630090, Russian Federation; [3]Department of Lithospheric Research, University of Vienna, Althanstraße 14/UZA2, Vienna, 1090, Austria; [4]Department of Earth Sciences, Utrecht University, Princetonlaan 8, Utrecht, 3584CB, The Netherlands

*Corresponding author, telephone +49-331-24366434, e-mail dirk@spengler.eu

Received 26 June 2020; Accepted 18 January 2021

ABSTRACT

Oriented lamellar inclusions of pyroxene and rutile in mantle garnet often serve as evidence for majoritic and titaniferous precursor garnets, respectively. We investigated ten new such microstructure-bearing samples from six orogenic peridotite bodies in SW Norway, which originated in the E Greenland mantle lithosphere, petrologically and thermobarometrically. All pyroxenite (nine) and eclogite (one) samples have large (mainly porphyroclastic) garnet containing silicate and oxide inclusions with shape-preferred orientation relationship. These inclusions vary—dependent on their size—systematically in shape (acicular to subprismatic), width (~50 μm to submicron size), spacing (several 100 to ~10 μm) and phase (pyroxene to Ti-oxide ± pyroxene). Smaller inclusions can fill the space between larger inclusions, which support the idea of consecutive generations. The larger, early formed lamellae occur least frequent and are most poorly preserved. A younger generation of other inclusions decorates healed cracks cutting across cores but not rims of garnet. These inclusions comprise oxides, silicates, carbonates (aragonite, calcite, magnesite) and fluid components (N_2, CO_2, H_2O). The older, homogeneously distributed inclusions comply texturally and stoichiometrically with an origin by exsolution from excess Si- and Ti-bearing garnet. Their microstructural systematic variation demonstrates a similar early evolution of pyroxenite and eclogite. The younger inclusions in planar structures are ascribed to a metasomatic environment that affected the subcratonic lithosphere. The microstructure-bearing garnets equilibrated at ~3.7 GPa (840 °C) and ~3.0 GPa (710 °C), at a cratonic geotherm related to 37–38 mW m^{-2} surface heat flow. Some associated porphyroclastic grains of Mg-rich pyroxene have exsolution lamellae of Ca-rich pyroxene and vice versa that indicate a preceding cooling event. Projected isobaric cooling paths intersect isopleths for excess Si in garnet at ~1550 °C, if an internally consistent thermodynamic data set in the system Na_2O–CaO–MgO–Al_2O_3–SiO_2 (NCMAS) is applied (or ~1600 °C if using CMAS). This temperature may confine the crystallisation of the unexsolved garnets at 100–120 km depths of the E Greenland subcratonic lithosphere. Tectonism is indicated in coastal and hinterland samples by porphyroclastic orthopyroxene with Al_2O_3 concentrations showing W-shaped profiles. Cores of associated large (>200 μm) recrystallised grains have low Al_2O_3 contents (0.18–0.23 wt.%). Both characteristics typify relatively short intracrystalline Al diffusion lengths and a prograde metamorphism into the diamond stability field. We assign this event to subduction during the Scandian orogeny. Porphyroclastic orthopyroxene in other samples shows U-shaped Al_2O_3 concentration profiles paired with long Al diffusion lengths (several 100 μm) that exceed the radius of recrystallised grains. Their cores contain high Al_2O_3 contents (0.65–1.16 wt.%), consistent with a diffusional overprint that obliterated prograde and peak metamorphic records. Unlike Al_2O_3, the CaO content in porphyroclastic orthopyroxene cores is uniform suggesting that early exhumation

was subparallel to Ca isopleths in pressure–temperature space. The depth of sample origin implies that rock bodies of Scandian ultra-high pressure metamorphism occur in nearly the entire area betweenNordfjord and Storfjord and from the coast towards ~100 km in the hinterland, i.e. in a region much larger than anticipated from crustal eclogite.

Key words: Caledonidesexsolution microstructuressubcontinental lithospheric mantleultra-high pressure metamorphismWestern Gneiss Region

INTRODUCTION

The Western Gneiss Region (WGR) in Norway exposes nearly twenty Mg–Cr garnet-peridotite bodies (Figure 1; Brueckner, 2018). These bodies have a two-fold history: their whole-rock chemistry points to an origin in the subcontinental lithospheric mantle (SCLM), while their entrapment in surrounding crustal gneiss indicates a late tectonic evolution (Carswell *et al.*, 1983; Brueckner, 1998). Many of these so-called orogenic (or mantle wedge) garnet-peridotites enclose layers and lenses of eclogite (sometimes referred to as 'internal eclogite'), garnet-pyroxenite and garnetite (Carswell, 1973; Lappin, 1973; Jamtveit, 1984; van Roermund & Drury, 1998). The latter two rock types can contain garnet with inclusions of pyroxene in the shape of lathy lamellae or rods that show a specific crystallographic orientation relationship to the garnet host (Spengler, 2006; Zhang *et al.*, 2011). This specific crystallographic orientation relationship as well as mineral microstructural characteristics, petrology and stoichiometry support the interpretation that the acicular microstructure formed by exsolution from majoritic garnet (van Roermund & Drury, 1998). Although, some samples have lamellar pyroxene with other crystallographic orientations to their host (Zhang *et al.*, 2011; Hwang *et al.*, 2013), which form the source for alternative interpretations. Radiogenic isotope data (Sm–Nd, Lu–Hf) of pyroxenite and garnetite containing the acicular microstructure record an isotopic equilibration in the form of isochron (or errorchron) relationships at mineral-scale within a long time interval, from the Mesoproterozoic to the early Palaeozoic (Brueckner *et al.*, 2002; Spengler *et al.*, 2006, 2009; Cutts *et al.*, 2019). However at whole-rock scale, geochronology yielded Palaeo- to Mesoarchaean ages at which crystallisation of pyroxenite and garnetite occurred. This crystallisation is virtually contemporaneous with a melt extraction event constrained by Re–Os isotope data of the harzburgitic to dunitic host peridotites and enclosed sulphides (Beyer *et al.*, 2004; Spengler, 2006). Such a synchrony of mantle rocks with

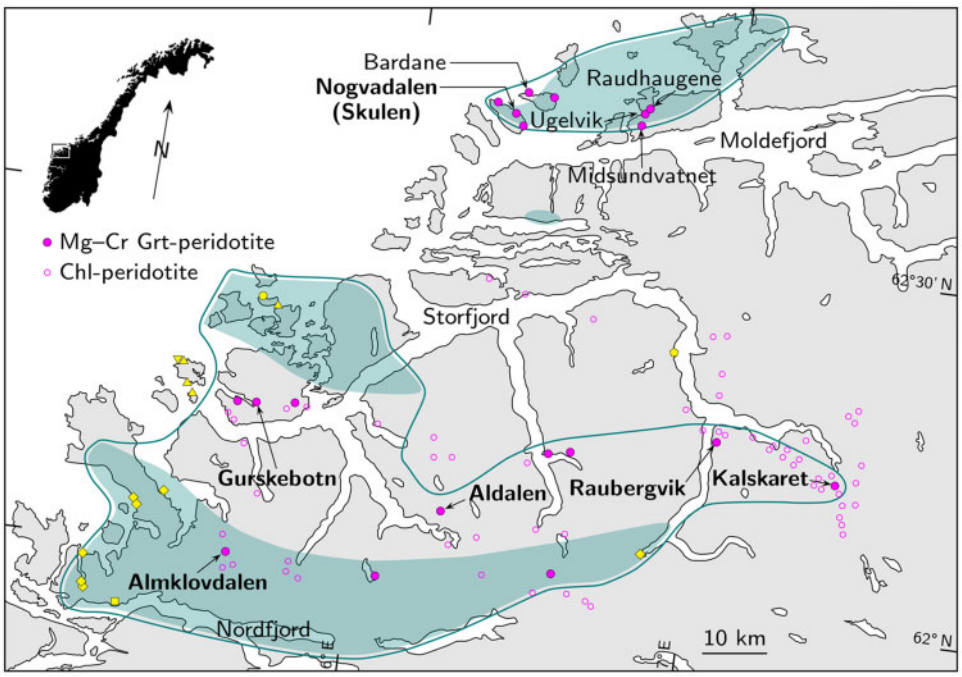

Figure 1: Overview map with locations of different types of peridotite bodies (magenta coloured symbols) in the WGR of Norway (adapted from Brueckner, 2018). Labelled bodies contain garnet with lamellar exsolution microstructures. Sample locations are marked in boldface. Areas containing UHP eclogite in gneiss are shaded in green (Smith, 1988; Spencer *etal.*, 2013). Areas that contain UHP eclogite and UHP peridotite in gneiss are outlined in green (this study). Other symbols refer to locations of orthopyroxene-eclogite, garnet-websterite and quartzofeldspathic rocks shown in Figure 13.

Table 1: Petrographic summary of WGR subcratonic pyroxenite and eclogite with modal proportions by volume of major minerals estimated by image analysis.

Sample	Locality latitude, longitude	Lithology	Modal proportions (vol.%)					Accessories	Recrys-tallisation	Type-A to -D inclusions in Grt
			Grt	Cpx	Opx	Ol	Amp			
DS1425	Aldalen 62.111 34°, 6.223 55°	eclogite	53	28	–	–	19	Rt	intense	Rt, Omp
DS0318	Alm.: Lien 62.002 91°, 5.609 60°	Grt-websterite	28	28	25	–	19	Rt, Ilm	moderate	Rt, Ilm, Opx, Cpx
DS1245	Alm.: Rødhaugen 62.007 97°, 5.640 85°	Grt-websterite	37	19	19	–	25	Rt	moderate	Rt, Cpx
DS1246	Alm.: Rødhaugen 62.007 97°, 5.640 85°	Grt-websterite	26	18	7	4	45	Rt, Ilm, Srp	moderate	Rt, Pyx
DS1249	Gurskebotn 62.218 24°, 5.654 18°	Grt-websterite	layered			–	<30	Rt	minor–moderate	Rt, Cpx
DS1252	Gurskebotn 62.218 24°, 5.654 18°	Grt-clinopyroxenite	39	36	3		22	Rt, Ilm, Chr, Srp	minor–moderate	Rt, Ilm, Chr, Opx
DS0466	Kalskaret 62.217 49°, 7.382 82°	Grt-websterite	49	21	9	–	21	Ilm	minor	Rt, Pyx
AH0364	Nogvadalen 62.680 05°, 6.304 31°	Grt-websterite	42	32	16	–	10	Ilm, Fe-sulphide	intense	Rt, Pyx
DS1201	Raubergvik 62.258 09°, 7.037 16°	Grt-websterite	14	41	15	–	30	Rt, Ilm	moderate	Rt, Ilm, Opx, Cpx
DS1225	Raubergvik 62.258 09°, 7.037 16°	Grt-websterite	2	49	28	–	21	Fe-sulphide	moderate	Rt, Pyx

Alm. = Almklovdalen.

fertile and melt depleted compositions suggests that the rocks with lamellar inclusions in garnet provide constraints on craton stabilisation mechanisms. For example, some pyroxenite and garnetite samples show such garnet to be associated with orthopyroxene that has exsolution lamellae of clinopyroxene and an Al-phase, which is either garnet or spinel (Carswell, 1973; Carswell & van Roermund, 2005; Spengler, 2006; Spengler *et al.*, 2019). The common occurrence of lamellae in garnet and orthopyroxene suggests a common origin for the exsolution microstructures in both minerals. This origin is constrained by the minerals' isopleths for Ca, Al and Si, which differ in slope in pressure–temperature *(P–T)* space (Fei & Bertka, 1999; Gasparik, 2000). More precisely, the solubility of Ca in orthopyroxene decreases with decreasing *T*, that of Al in orthopyroxene with decreasing *T* and/or increasing *P* and that of Si in garnet with decreasing *T* and/or decreasing *P*. By implication, the exsolution of Ca- and Al-phases from orthopyroxene, concurrent with silicate exsolutions in garnet, requires a near isobaric cooling (Spengler & Alifirova, 2019). Therefore, the acicular microstructure can be taken as indicator for an event at high *T*. However, occurrences of this microstructure are known from a few ultramafic bodies only which have barely been compared with each other.

Garnet in these ultramafic bodies can additionally include oriented acicular inclusions of oxides, which are dominantly rutile and ilmenite (van Roermund *et al.*, 2000a, 2017; Katayama *et al.*, 2005; Cuthbert & van Roermund, 2010). It is possible that all these kinds of inclusions occur also in garnet of the embedding peridotites (Hwang *et al.*, 2013), which may have formed by mechanical mixing of dunite and garnet-pyroxenite during intense deformation (Spengler *et al.*, 2018). The timing of this deformational event (Spengler *et al.*, 2009) coincides with the Scandian orogeny (Griffin & Brueckner, 1980), which is believed to have incorporated mantle fragments from the hanging wall into subducted continental crust (Brueckner, 1998) and associated ultra-high pressure (UHP) metamorphism (Smith, 1984; Carswell & Cuthbert, 2003). UHP metamorphic conditions have also been found in dynamically recrystallised mantle mineral assemblages (Carswell *et al.*, 2006; Spengler, 2006). Consequently, some of the WGR orogenic peridotite bodies are UHP metamorphic records of Caledonian continent–continent collision. Nevertheless, the significance of quantified peak metamorphic *P* from both crustal and mantle units is disputedrecently concerning theoretical concepts (Vrijmoed *et al.*, 2009; Cutts *et al.*, 2020) and subduction models (Liu & Massonne, 2019).

This study focuses on ten new samples of pyroxenite and eclogite from six peridotite bodies (Aldalen, Almklovdalen, Gurskebotn, Kalskaret, Nogvadalen, Raubergvik; Figure 1; abbreviations for minerals follow the recommendation of Whitney & Evans, 2010, with the addition of CaTs for Ca-Tschermak's pyroxene and Pyx for pyroxene; the term Pyx denotes in Table 1 and Figure 3 crystals that were not determined for composition and refers to sample dependent pyroxene compositions otherwise). Petrological and thermobarometric studies on these samples have two objectives: (1) to describe the variation of the most typical inclusion types in garnet and (2) to investigate the mineral-chemical evolution for evaluating the tectono-metamorphic

significance of the mantle rocks. The aim of the first objective is to provide new constraints on the origin of oriented inclusion microstructures in mantle garnet. That of the second is to explain on why mantle garnet-peridotites occur within and in between known UHP areas (Figure 1).

GEOLOGICAL SETTING AND SAMPLE LOCALITIES

The WGR in SW Norway exposes high-grade metamorphic rocks with Proterozoic protolith ages (Kullerud *et al.*, 1986; Tucker *et al.*, 1990) representing the western margin of Baltica (Gee *et al.*, 2013). These rocks, Proterozoic basement gneisses, together with minor infolded supracrustal rocks (Krill, 1980) were reworked during the Caledonian orogeny and form the lowermost tectono-stratigraphic unit of a nappe pile, which is known as the Scandinavian Caledonides. The nappes were thrust onto the Baltic Shield during the Early Palaeozoic closure of the Iapetus Ocean and the subsequent continent–continent collision, called the Scandian phase (~430–375 Ma; Tucker *et al.*, 2004; Corfu *et al.*, 2014). The margin of western Baltica was subducted underneath eastern Laurentia during the climax of this collision. Studies on eclogite ('external eclogite') enclosed in WGR gneiss assign this burial to have resulted in UHP metamorphism of eclogite and by inference to deeply subducted gneiss (Smith, 1984; Root *et al.*, 2005; Hacker, 2006; Smith & Godard, 2013). Cofacial UHP metamorphism of eclogite and gneiss is also consistent with the findings of coesite in detrital garnets of high-grade metamafic and metasedimentary affinities (Schönig *et al.*, 2018), whereas studies on WGR gneiss gave contrasting results in some cases (Dobrzhinetskaya *et al.*, 1995; Liu & Massonne, 2019). Chronological data suggest long-lasting, perhaps multiple burial for a few tens of million years (Griffin & Brueckner, 1985; Tucker *et al.*, 2004; Kylander-Clark *et al.*, 2007, 2013; Spengler *et al.*, 2009; Walczak *et al.*, 2019). The process of (U)HP metamorphic Baltica crust exhumation is disputed. Metamorphic gradients of gneiss-hosted eclogite (Krogh, 1977; Griffin et al., 1985; Hacker et al., 2010) and the lack of major deformation apart from peak metamorphic areas and regional shear zones (Hacker *et al.*, 2013; Spencer *et al.*, 2013; Kylander-Clark & Hacker, 2014; Young, 2018) suggest the WGR gneiss exposure to form—and thus to have been exhumed as—internally largely coherent gneiss units. Alternatively, ductile reverse flow as characteristic for numerically modelled subduction channels may apply (Warren *et al.*, 2008). The minimum exhumation depth of gneiss is suggested by quartz pseudomorphs after coesite (Wain, 1997). The maximum exhumation depth of gneiss depends on the applied metamorphic concept and subduction model. For instance, if the mineral chemistry records lithospheric *P*, then exhumation of UHP eclogite and peridotite in cofacial gneiss can be traced from the deep diamond stability field (up to ~200 km depth; Cuthbert *et al.*, 2000; Spengler *et al.*, 2009). Alternatively, if tectonic overpressure was relevant during UHP metamorphism (Vrijmoed *et al.*, 2009), then it is possible that continental exhumation has been limited to the onset of the diamond field (~120 km; Cutts *et al.*, 2020). Whereas if eclogite and mantle peridotite evolved decoupled from the Baltica plate margin in channel flows then their metamorphism can be unrelated to that of gneiss (Liu & Massonne, 2019).

All these tectono-metamorphic variants share that deep subduction of the Baltica margin and the adhered oceanic crust entrained fragments from the overriding Laurentian mantle wedge (Brueckner, 1998), i.e. the SCLM of the eastern Rae craton (St-Onge *et al.*, 2009). Palaeogeographical reconstructions locate the provenance of the ultramafic rocks prior to their recrystallisation at ~430 Ma (Spengler *et al.*, 2009) underneath present 69°N of central E Greenland (Cocks & Torsvik, 2005). This area became at ~60 Ma affected by lithosphere delamination and modification related to the Greenland passage over the Isand plume (Steinberger *et al.*, 2019). The tectonically transported SCLM fragments are now, after orogen relaxation, exposed as orogenic peridotite bodies across wide areas in the WGR (Figure 1; Brueckner, 2018). Individual bodies vary in size from a few metres to a few kilometres. Detrital zircon, interpreted to be derived from the ultramafics, has trace-element and isotope signatures in support of a Laurentian provenance (Beyer *et al.*, 2012). Garnetiferous bodies enclose variable proportions of layers and lenses of eclogite, garnet-pyroxenite and garnetite. These enclosures vary in dynamic recrystallisation (from virtually zero to complete) and fragmentation caused by Scandian shear deformation (Spengler *et al.*, 2009, 2018). Shear-induced mechanical mixing of fragmented pyroxenite and garnetite with the embedding melt-depleted peridotite may have transformed initially garnet-poor or garnet-free peridotite into garnet-bearing peridotite, a process that was also found to have modified Laurentian mantle fragments exposed in the Greenland Caledonides (Brueckner *et al.*, 2018).

The above mentioned oriented pyroxene inclusions in garnet were reported only from grains and grain fragments that resisted the overall dynamic recrystallisation. Though, the proportion of oriented inclusions preserved in these garnets can largely vary between grains within a single sample. The first reports of lamellar pyroxene in garnet were from the Raudhaugene and Ugelvik bodies (Otrøy; van Roermund & Drury, 1998) and from occurrences at Bardane (Fjørtoft) and Nogvadalen, a sloping valley approximately 600 m NW of the Skulen summit (Flemsøy; Terry *et al.*, 1999). Subsequent locations were Midsundvatnet (Otrøy; Spengler, 2006), Raubergvik (Cuthbert & van Roermund, 2010) and the Gusdal quarry within the Almklovdalen body (Spengler *et al.*, 2019). Three samples described in this study are from these locations: Nogvadalen (one) and Raubergvik (two). The other seven samples are from locations that were not known

to preserve oriented pyroxene inclusions in garnet prior to this study: the Rødhaugen (two) and Lien (one) outcrops of the Almklovdalen body, Aldalen (one), Gurskebotn (two) and Kalskaret (one).

The two Rødhaugen samples are from garnet-pyroxenite layers, which occur with different thickness at this locality, a few cm to a few dm. Sample DS1245 was taken directly from the outcrop, whereas DS1246 is a loose piece lying close to an exposed garnet-pyroxenite layer. The Lien sample (DS0318) is part of a folded garnet-pyroxenite layer, which has a maximum thickness of ~50 cm. Both Raubergvik samples (DS1201, DS1225) were taken from loose, blasted rocks dumped along the road connecting the entrance of the Raubergvik mine and the nearby harbour. The Nogvadalen sample (AH0364) was taken from a pyroxenite layer exposed at the lower part of the peridotite exposure. The Aldalen sample (DS1425) is part of a loose block approximately $2 \times 1.5 \times 1.5$ m^3 in size of massive, ductily folded eclogite. This block is located downhill below the western edge of the northern peridotite exposure at Aldalen, i.e. in the forest about 100 m ESE from the Aldalsvegen junction to Ullalandssætra farmhouse. The position of the massive eclogite block at the bottom of a hill suggests that its original position was further uphill within the northern peridotite exposure. Thus, the eclogite should be an 'internal eclogite'. The two hand specimens from the Gurskebotn body were taken from an outcrop at the foot of the cliff in Vågen: sample DS1249 is part of a pyroxenite layer thicker than 35 cm; sample DS1252 is an 8 cm thick pyroxenite layer. The Kalskaret sample (DS0466) is from the easternmost occurrence of garnet-websterite layers within the Kalskaret garnet-peridotite body.

A recent study suggests that several garnet-peridotite bodies across the WGR share a common tectonometamorphic evolution from the Archaean to the early Scandian (Spengler *et al.*, 2019). We follow this approach and apply the same nomenclature to ascribe the different mineral generation in our sample suite. Minerals that formed prior to the oriented inclusions are assigned to M1. Minerals that host these oriented inclusions (i.e. the non-recrystallised, mostly porphyroclastic grains) and those that share the same texture but lack oriented inclusions (porphyroclasts) are related to M2. Dynamically recrystallised minerals, which replace M2 grains, are assigned to M3.

METHODS

Major and minor element concentrations in minerals were analysed using a CAMECA SX-100 electron microprobe (EMP) equipped with five wavelength dispersive spectrometers (WDS) at the Institut für Mineralogie und Kristallchemie (now at Institut für Anorganische Chemie), Universität Stuttgart. Operating conditions were 15 kV acceleration voltage, 15 nA beam current, a focused beam size, 20 s counting time per element at the peak position in WDS mode and 10–20 s at the background. Obtained data were corrected using the ZAF routine. External calibration occurred against international oxide and silicate standards.

Raman micro-spectroscopy was conducted on thin sections made from the garnet-pyroxenite and eclogite samples to identify crystalline and fluid phases in inclusions. The Raman analyses were obtained with a Horiba Jobin Yvon LabRam HR (high resolution) 800 mm spectrometer, coupled with a Nd:YAG 532 nm excitation wavelength laser and an Olympus BX41 microscope, at the Sobolev Institute of Geology and Mineralogy of SB RAS (IGM), Novosibirsk. The laser beam was focused either at or beneath the surface of the samples with an approximate diameter of 1–2 μm and at 5–30 mW laser power. The Raman spectra were recorded at room temperature in the backscattering geometry with an Olympus MPlan 100× objective lens (0.37 mm working distance, 0.9 numerical aperture). A Peltier-cooled charge coupled device (CCD) detector was utilised for data collection. Accumulation time was generally 50 s. To extract peak positions, a least-squares curve was fitted to the baseline-corrected Raman spectrum using combined Gaussian functions. Calculation precision was about ±0.2 cm^{-1}. The spectral resolution for the recorded Stokes-side Raman spectrum was set to ~2 cm^{-1} achieved by usage of 1800 grooves per mm gratings and 200 μm slits. The system was calibrated using the 520.7 cm^{-1} Raman band of silicon before and after each experimental session. Raman spectra of the minerals were compared with relevant ones from the open access RRUFF database (Lafuente *et al.*, 2015) and published data.

Mineral modes were estimated from thin sections ~150 μm thick, which were electronically scanned and subsequently processed for quantitative 2D digital image analysis using the software GIMP (version 2.8, https://www.gimp.org). Original RGB images with a resolution of 107–142 px mm^{-1} were first converted to indexed images using the conversion function of the software in combination with colour palettes. These palettes were individually defined for each sample by selecting 39–89 colour shades from the major minerals of each scanned image. Subsequently, proportions of pixels with mineral specific colours were determined from the indexed images using the histogram function of the software applied to areas 300–550 mm^2 in size. Areas that included grain boundaries, cracks and oxides accounted for 1–38 % of an individual image and were ignored. Area percentages of minerals were assumed to be equal to the proportion of their volume percentages, i.e. the mineral modes of the rock.

RESULTS

Petrography

Inclusion types

All ten samples contain garnet with inclusions and were affected by recrystallisation resulting in the reduction of the grain size. The degree of recrystallisation varies from minor to intense (Table 1, Figure 2). Only non-

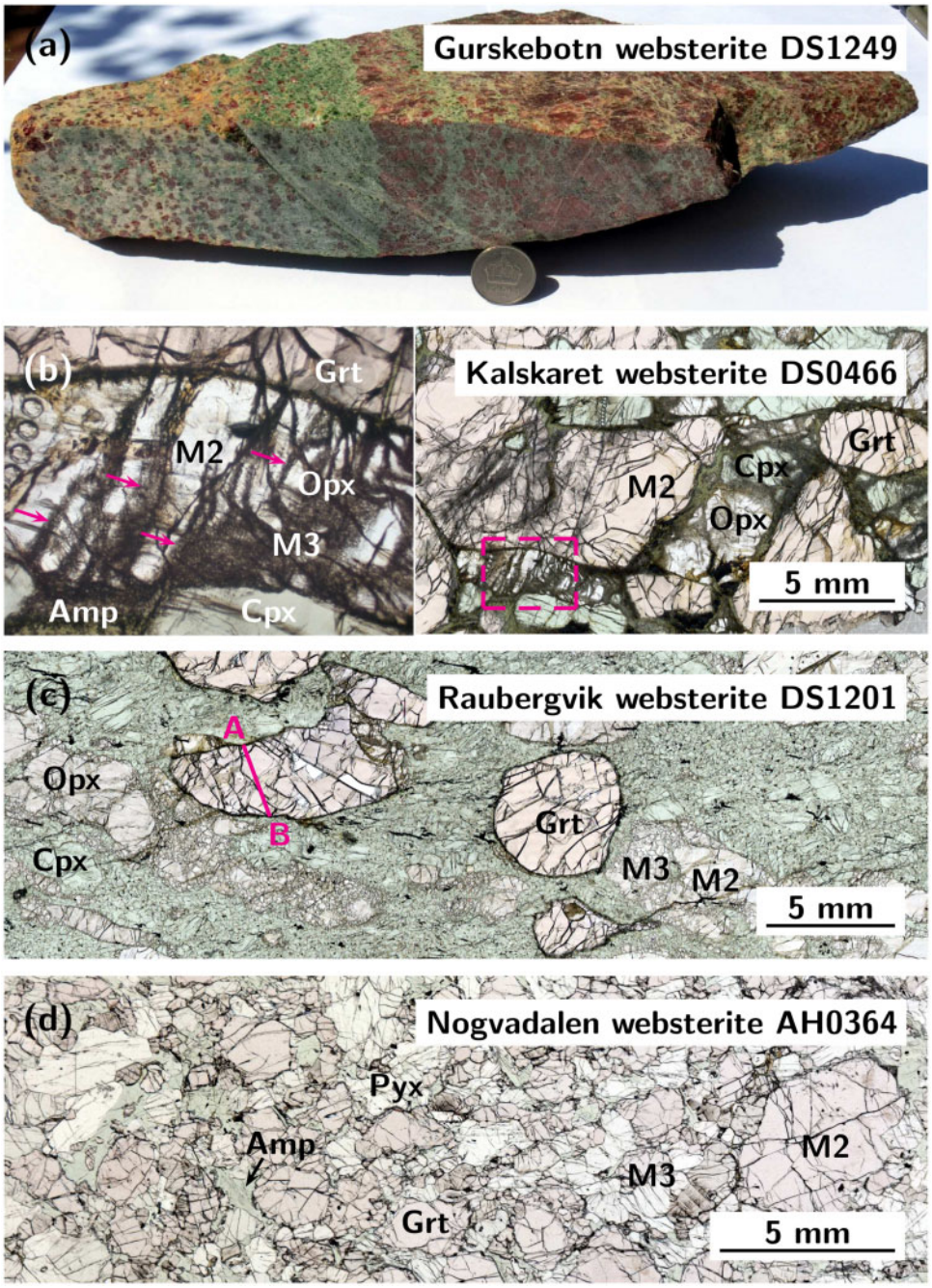

Figure 2: Variation of rock texture in WGR subcratonic pyroxenite (sample details are given in each panel). (a) A mineralogically layered hand specimen shows gradual and sharp transitions between orthopyroxene-rich, clinopyroxene-rich and garnet-rich layers (from left to right; daylight image). Coin for scale = 2.5 cm. (b) A granoblastic (M2) microstructure showing minor recrystallisation (M3) along selected grain boundaries and crystal transects (arrows; scanned thin section, framed area denotes the position of the inset shown on the left with ablation craters for scale = 150 μm). (c) A porphyroclastic microstructure after moderate recrystallisation contains all major mineral phases as M2 porphyroclasts, but the original grain contacts are erased by the dynamic recrystallisation process into M3 grains (scanned thin section). (d) Enlargement of a microstructure after intense M3 recrystallisation; only garnet is preserved as M2 porphyroclasts (scanned thin section).

recrystallised garnet grains contain inclusions. These inclusions vary in size, shape, phase, associated phase, distribution and shape-preferred orientation relationship with the host garnet crystal, but are comparable within the sample suite. Variation systematics allows a subdivision of the inclusions into six types, which are summarised in Table 2 and are described below. Several types of inclusions can occur together within single garnet grains. Many non-recrystallised garnets lack inclusions.

Type-A Thick lamellae (or rods) of pyroxene (omphacite in eclogite, clinopyroxene in pyroxenite) show

cross-sectional surfaces of 40–60 μm in width and >1 mm in length. Grain boundaries are usually straight but curvaceous in sections. The rare pyroxene rods show a spacing of several 100 μm and seem to have a shape-preferred orientation relationship with the host garnet (Figure 3a–c).

Type-B Thin lamellae of pyroxene and rarely ilmenite, which are mostly 5–20 μm in width and several 100 μm in length, show straight grain boundaries. The rare lamellae with a distance of several 100 μm show a shape-preferred orientation relationship with the garnet host (Figure 3d–f).

Type-C Short- to long-prismatic rods of mainly rutile, subordinately ilmenite and rarely chromite are dominantly 1–2 μm in width, 10–100 μm in length and occur spatially associated with minor pyroxene inclusions. These inclusions are either short-prismatic platelets, grains or rods, all of which are a few microns in dimension (1–15 μm). Individual inclusions of oxides and pyroxene occur mono-mineralic or intergrown, show shape-preferred orientation in the garnet host, a spacing of several 10 μm and a spatially uniform distribution (Figure 3c, g–m).

Type-D Frequent submicron-sized subprismatic and equant grains of mainly rutile and minorly ilmenite (inferred) and pyroxene (inferred), which show a spacing of approximately 10 μm, are uniformly distributed (Figure 3g–m, p).

Type-E Approximately micron-sized, subprismatic grains of rutile decorate curvilinear structures (dislocations; Figure 3r).

Type-F Short-prismatically to irregularly shaped, mutually comparable inclusions of a variety of minerals are concentrated within planar, subparallel, slightly curvaceous structures (healed cracks) that transect cores but no rims of garnet. The inclusions appear lined-up in thin sections, can be associated with a halo of depletion of inclusions in the host garnet and have no noticeable preferred orientation. Individual inclusions vary in size between a few microns and 50 μm, occur as single phases or as polyphase mineral assemblages and comprise carbonates (aragonite, calcite, magnesite), fluids (CO_2, H_2O, N_2), silicates (amphibole, serpentine, clinopyroxene, olivine, orthopyroxene) and oxides (rutile, ilmenite, chromite; Figure 3n–q).

Sample description

Eclogite Sample DS1425 is an eclogite mainly composed of garnet (53 vol.%) and omphacite (28 vol.%). Porphyroclastic, 1–4 mm sized garnet dominates the rock texture; minor omphacite porphyroclasts are usually <1 mm in dimension. These M2 porphyroclasts occur within a foliated groundmass of M3 recrystallised garnet and omphacite grains, which are dominantly 0.1–0.5 mm in diameter. M3 omphacite has grain margins replaced by symplectite usually <50 μm in width. Secondarily formed amphibole (19 vol.%; post-M3) partially replaced omphacite. Many matrix minerals enclose minor rutile grains.

Porphyroclastic garnet is birefringent and can contain different types of oriented inclusions. The largest inclusions (Type-A) are omphacite (Figure 3a–c) with straight or curvaceous grain boundaries (on the left in Figure 3b). Only a few garnet grains have this kind of lamellae. Rare garnet shows that these lamellae are widely spaced (several 100 μm; Figure 3b). Type-B pyroxene inclusions of presumed omphacite composition appear sporadically as widely spaced lamellae (several 100 μm) with straight grain boundaries (Figure 3d). Short-prismatic Type-C rutile inclusions occur partially associated with both types of large pyroxene lamellae (Type-A and Type-B; Figure 3c). Rods of Type-C inclusions consist of either rutile or a composite of rutile and minor pyroxene of presumed omphacite composition. Submicron-sized Type-D inclusions of rutile and a minor component inferred by optical light microscopy to be pyroxene occur in between Type-C inclusions (inset in Figure 3c). Furthermore, Type-F inclusions in garnet are 1–10 μm in size, occur as single phases and polyphase assemblages and include calcite, magnesite and CO_2 (Figure 4). Omphacite porphyroclasts contain lamellar oxides ~1 μm in width, which are oriented parallel to each other. Recrystallised garnet and omphacite grains lack oriented inclusions.

Garnet-pyroxenite The pyroxenites have variable mineral modes (Table 1). Two samples from Raubergvik show low garnet modes (2–14 vol.%) and high clinopyroxene modes (41–49 vol.%). Orthopyroxene contents are intermediate (15–28 vol.%). Six samples from Almklovdalen, Gurskebotn, Kalskaret andNogvadalen contrast with high, medium and low proportionsof garnet (26–49 vol.%), clinopyroxene (18–36 vol.%) and orthopyroxene (<3–25 vol.%), respectively. Unlike all other samples, DS1249 (Gurskebotn) shows a major mineralogical layering (Figure 2a). Individual layers vary in composition betweenorthopyroxene-rich garnet-websterite (e.g. Grt_{32}–Cpx_{20}–Opx_{46}–Amp_3; subscript numbers refer to vol.%), orthopyroxene-poor garnet-websterite (e.g. Grt_{21}–Cpx_{28}–Opx_{22}–Amp_{29}), garnet-clinopyroxenite and garnetite (from left to right in Figure 2a). Mineral modes at the transition of these rock types can change gradually or sharply. Minor amounts of olivine (<5 vol.%) occur in only two out of nine pyroxenites. All handspecimens are classified as garnet-websterite except sample DS1252 (Gurskebotn), garnet-clinopyroxenite. Late amphibole (up to 45 vol.%) occurs locally concentrated at grain boundaries and partially replaced pyroxene (dominantly) and garnet (subordinately).

The rock texture is porphyroclastic (Figure 2c, d) except for the Kalskaret pyroxenite, granoblastic (Figure 2b). Three samples with low proportions of recrystallisation (i.e. from Gurskebotn and Kalskaret; Figure 2a, b) preserve original contacts between some M2 grains, which show equilibrated grain boundary angles of ~120°. The degree of recrystallisation in these three samples varies and is locally concentrated along grain boundaries and planes that transect large crystals (arrows in Figure 2b), but the overall rock texture is

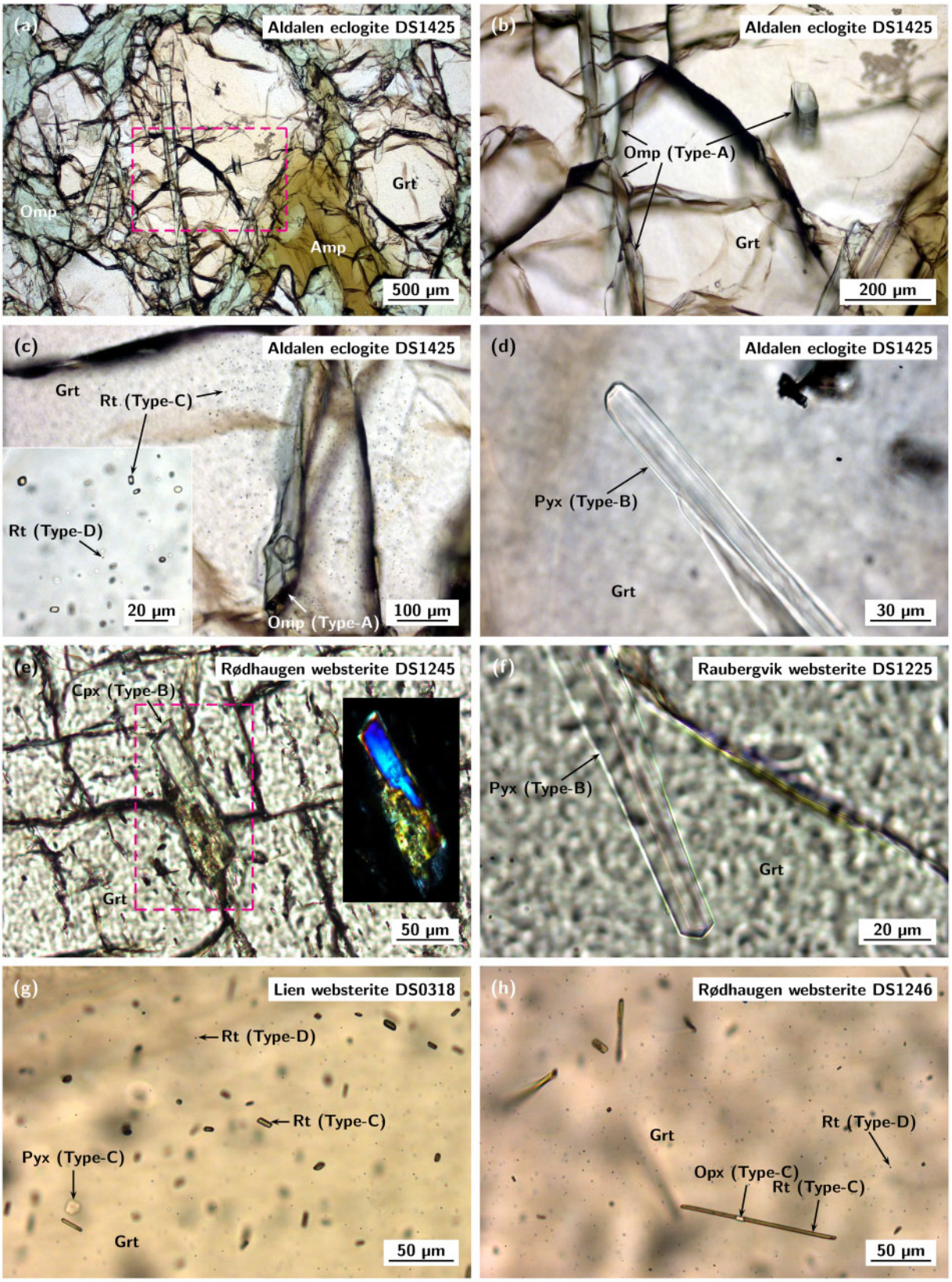

Figure 3: Microstructures of mineral inclusions in M2 garnet (a–r, plane-polarised light images) and clinopyroxene (s, cross-polarised light image) from WGR subcratonic pyroxenite and eclogite (sample details are given in each panel). (a) Thick omphacite lamellae (Type-A). (b) Magnified garnet core area framed in panel a. (c) Short-prismatic rutile grains (Type-C) surround a thick omphacite lamella (Type-A). The inset magnifies rutile (Type-C and -D) in garnet. (d) Thin pyroxene lamella (Type-B). (e) Thin clinopyroxene lamella partially replaced by alteration (Type-B). The inset shows the lamella photographed using crossed polarisers. (f) Thin pyroxene lamella (Type-B). (g) Submicron-sized, isometric to subprismatic rutile grains (Type-D) are located in between

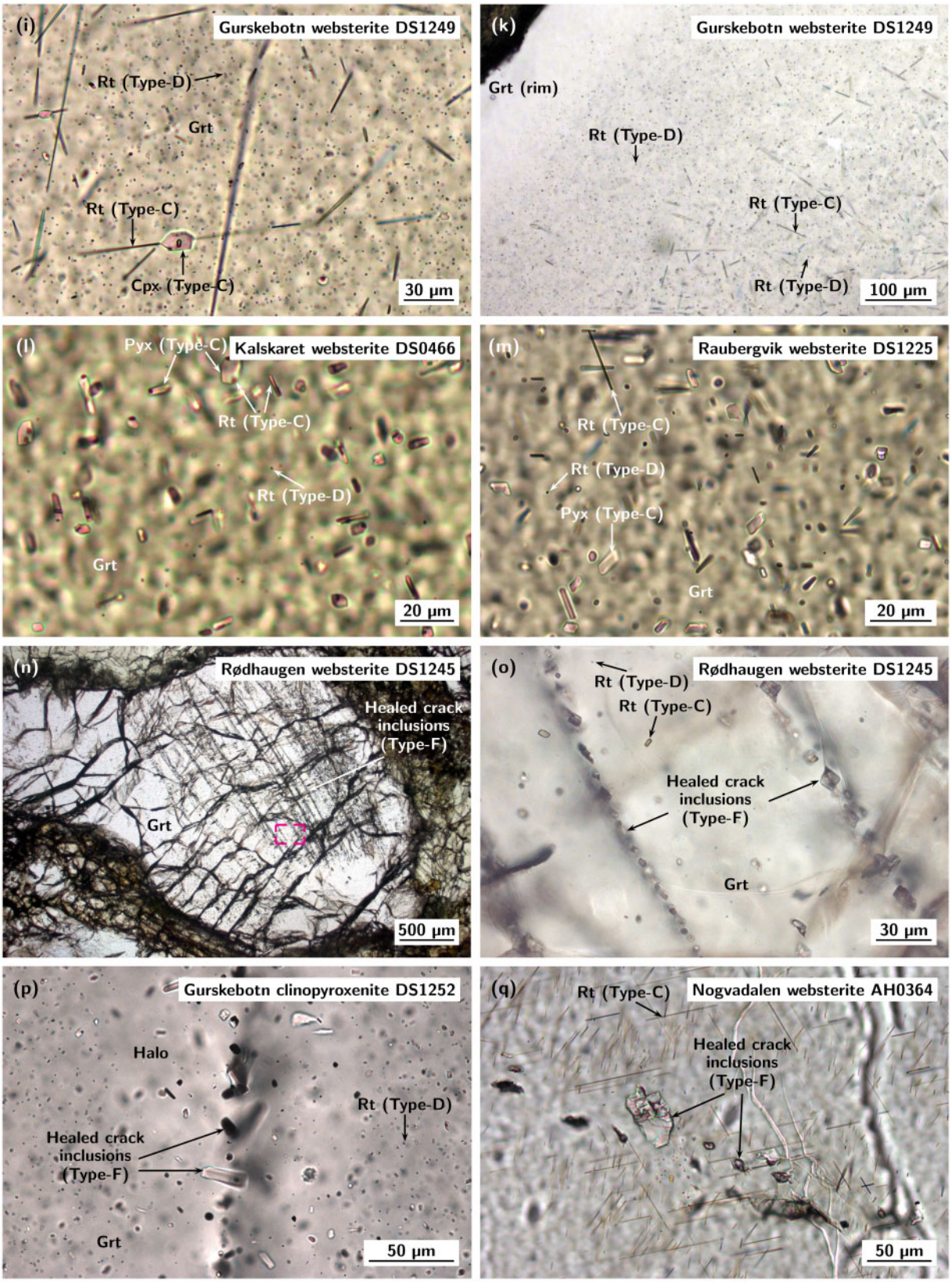

Figure 3: Continued. micron-sized rods and plates of short-prismatic rutile and pyroxene (Type-C). (h, i) Submicron-sized rutile grains (Type-D) occur in between micron-sized rods (long-prismatic) of rutile closely associated with ortho- and clinopyroxene (Type-C). (k) A garnet core shows inclusions of Type-C and -D, the adjacent area of Type-D and the rim area is inclusion-free (from lower right to upper left). (l) Type-D rutile occurs in between composite inclusions of micron-sized rutile and pyroxene (Type-C). (m) Type-D rutile occurs in between single phase inclusions of micron-sized rutile rods and pyroxene platelets (Type-C). (n) Inclusion-rich healed cracks transect the core but not the rim of garnet (Type-F). (o) Inclusions within healed cracks appear lined-up along subparallel directions (Type-F) unlike regularly distributed inclusions (Type-C and -D; magnified area framed in panel n). (p) Inclusions

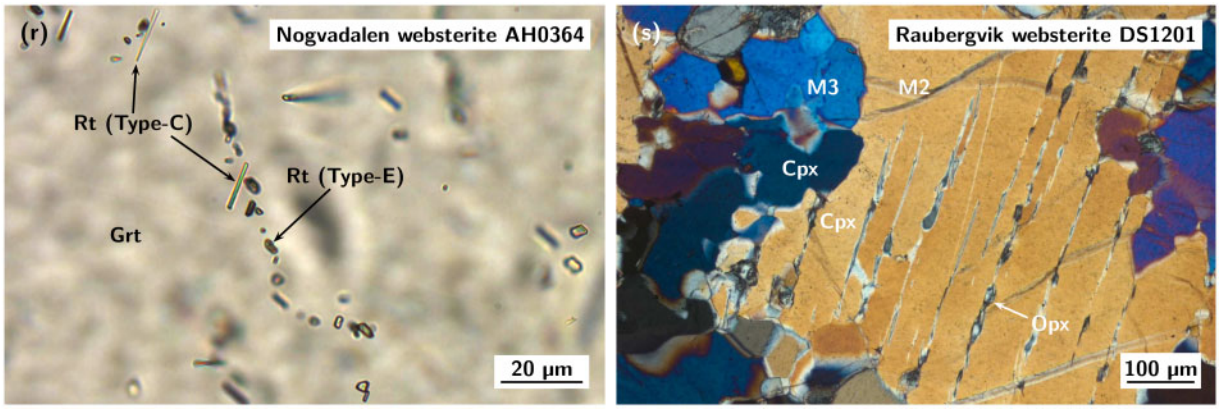

Figure 3: Continued. (Type-F) in a healed crack show a halo depleted in tiny Type-D inclusions. (q) Inclusion (Type-F) in a healed crack transect an area with long-prismatic Type-C inclusions. (r) Short-prismatic rutile inclusions (Type-E) strung together along an inferred dislocation in garnet occur in between oriented rutile rods (Type-C). (s) Lamellae of orthopyroxene in porphyroclastic M2 clinopyroxene.

Table 2: Summary of inclusion types in garnet of WGR subcratonic pyroxenite and eclogite.

Type	Mineral (thickness)	Distribution	Aldalen	Alm.: Lien	Alm.: Rødhaugen	Gurskebotn	Kalskaret	Nogvadalen	Raubergvik
A	Pyx (40-60 μm)	uniform	•		•				
B	Pyx ± Ilm (5-20 μm)	uniform	•		•	•		•	•
C	Rt ± Ilm ± Chr ± Pyx (1-5 μm)	uniform	•	•	•	•	•	•	•
D	Rt ± Ilm ± Pyx (<1 μm)	uniform	•	•	•	•	•	•	•
E	Rt (~1 μm)	dislocations						•	
F	Silicates, carbonates, oxides, fluid inclusions (1-50 μm)	healed cracks	•		•	•	•	•	

Alm. = Almklovdalen.

unfoliated, except for sample DS1252 that has a foliated matrix. The other six samples show higher proportions of recrystallisation with clearly foliated textures being typical for dynamic recrystallisation (Figure 2c, d). All pyroxenites contain M2 grains mostly 1–10 mm in size, but garnet grains can be larger, 15 mm. M2 pyroxene and M2 olivine often show undulose extinction indicating intense strain. M2 garnet is typically birefringent and—in olivine-bearing samples—decorated by a fine-grained kelyphite corona 0.1–0.2 mm thick. Serpentine partially replaces olivine. M2 grains locally contain subprismatic inclusions (0.05–1 mm in diameter) of pyroxene, olivine and accessory phases (see Table 1) in garnet—and garnet and accessories in pyroxene. The M2 porphyroclasts are embedded in a recrystallised matrix of M3 grains (mostly 0.1–0.3 mm in size) of clino- and orthopyroxene, minor garnet, a few oxides and rare olivine. M3 pyroxene is largest (0.1–1 mm) in the most intense recrystallised sample (Nogvadalen; Figure 2d), but smallest (10–100 μm) in recrystallised bands of the least recrystallised (granoblastic) sample (Kalskaret; Figure 2b).

M2 pyroxene cores can contain parallel rods and/or lamellae of oxides and/or silicates (Ca-rich pyroxene in Mg-rich pyroxene and vice versa), which are submicron to micron in width for oxides and up to a few microns in width for silicates (Figure 3s). Depending on the sample site, M2 garnet cores show variable combinations of Type-A to Type-D inclusions (Table 2). Each combination includes Type-C and Type-D and is a continuous sequence of consecutive inclusion sizes. Large lamellae (Type-A and Type-B) in individual grains occur spatially associated with or without the smaller Type-C and Type-D inclusions and show alteration to different extent (Figure 3e, f). Type-D inclusions either fill the space in between Type-C ones (Figure 3g–m) or occur without them (Figure 3k). Type-E (Figure 3r) has been found only in the sample with the highest degree of recrystallisation (Nogvadalen). Characteristic for inclusions of Type-C, -D and -E is their occurrence in domains of M2 garnet. These domains may cover the whole garnet core or only parts of it. Type-F (Figure 3n–q) inclusions were found in samples from every body except Raubergvik. These inclusions, which decorate planar, subparallel and slightly curvaceous structures, can show a halo ~50 μm in width that is depleted in submicron-sized inclusions (Figure 3p). Original garnet rims are inclusion-free (Figure 3k, n). In general, inclusions

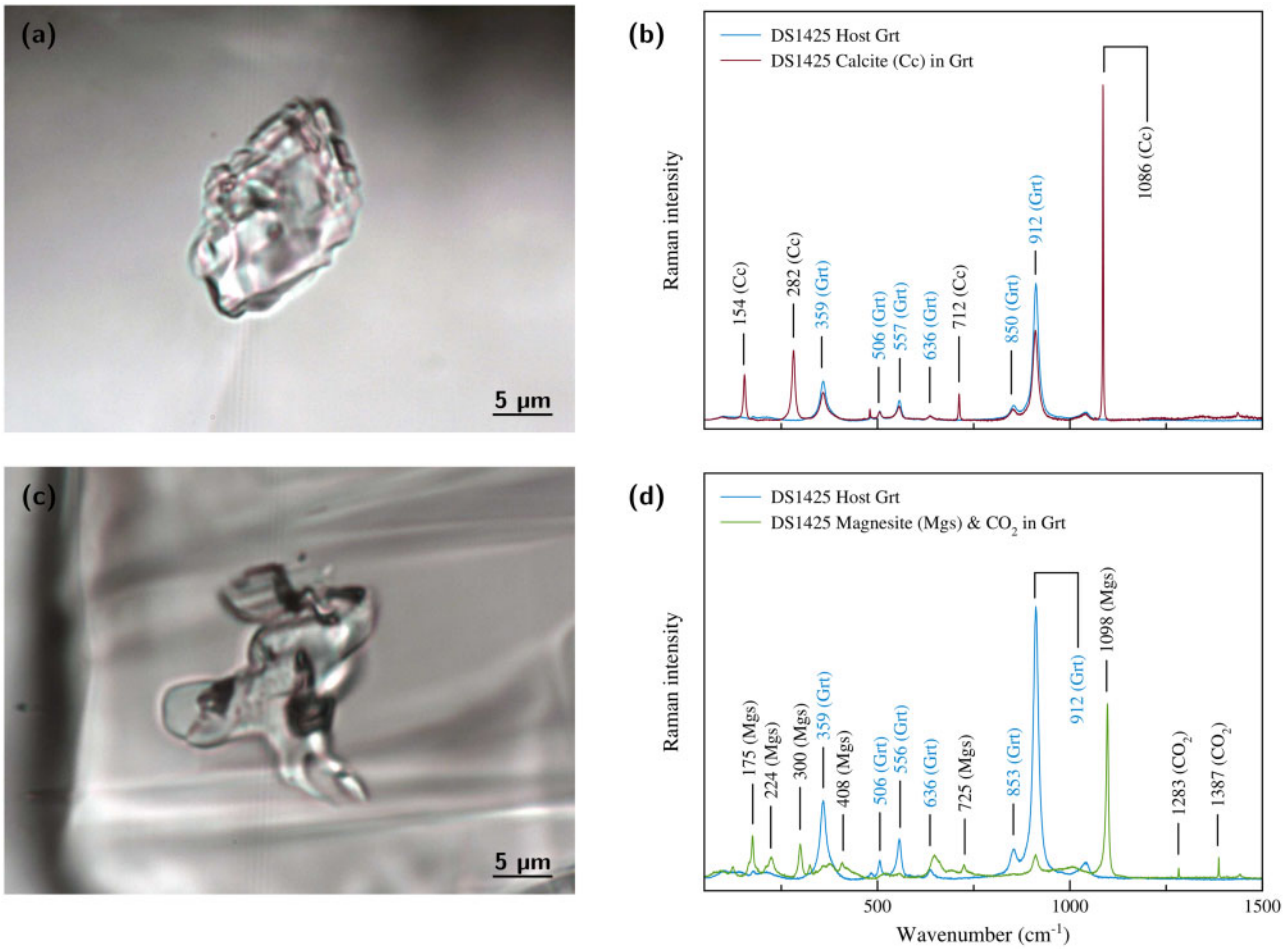

Figure 4: Selected F-Type inclusions in healed cracks in Aldalen eclogitic garnet (DS1425). (a) Optical photograph of a monophase inclusion. (b) Raman spectra of the inclusion shown in panel a. (c) Optical photograph of a multicomponent inclusion. (d) Raman spectra of the inclusion shown in panel c.

disappear consecutively from core to rim, the larger ones first, the submicron-sized last (Figure 3k).

Mineral chemistry

Garnet

Porphyroclastic M2 garnet in all rock types is compositionally zoned. A decrease of MgO and an increase of FeO from core to rim is most prominent (Figure 5).

The eclogite M2 garnet cores contain in average $Prp_{38}Alm_{35}Grs_{26}Sps_1$ (subscript numbers refer to mol%, Figure 6, Supplementary Data Electronic Appendix 1; supplementary data are available for downloading at http://www.petrology.oxfordjournals.org). Contents of Cr_2O_3 and TiO_2 are 0.08 wt.% and 0.05 wt.%, respectively. The Mg# = $Mg/(Mg+Fe^{total})$ value is 0.503. The classification scheme of Grütter *et al.* (2004) describes this garnet as eclogitic (G3; Figure 7). M3 recrystallised garnet is chemically homogeneous $Prp_{39}Alm_{38}Grs_{22}Sps_1$. Cr_2O_3 and TiO_2 contents are below the analytical detection limit. The Mg# number is 0.497.

Porphyroclastic garnet cores in the pyroxenites are pyropic but variable in composition, $Prp_{49–71}Alm_{17–38}Grs_{7–11}Sps_1Uv_{1–4}$ (Figure 6). Cr_2O_3 and TiO_2 contents are higher than in the eclogite and range from 0.29 to 1.32 wt.% and from 0.05 to 0.14 wt.%, respectively, except for garnet in sample DS1245 that shows a TiO_2 content below the detection limit. The Mg# values are between 0.555 and 0.803. Garnet from Almklovdalen, Kalskaret, Nogvadalen and Raubergvik is pyroxenitic (G4 and G5) and that from Gurskebotn lherzolitic (G9; Figure 7). The recrystallised grains of garnet in the Nogvadalen sample are compositionally zoned in thesame fashion as the porphyroclastic rims. The coresof these M3 garnet grains are pyropic too, $Prp_{65}Alm_{21}Grs_{10}Sps_1Uv_3$, and show Cr_2O_3 and TiO_2 contents of 0.98 wt.% and $<$0.03 wt.%, respectively. Mg# is 0.748.

Clinopyroxene

Porphyroclastic M2 clinopyroxene is usually compositionally zoned. Most dominant is a decrease of the Al_2O_3, Na_2O and TiO_2 contents and an increase of the CaO and MgO contents from core to rim (Figure 8a). However, many crystals were found to be irregularly zoned (Figure 8b). The composition of recrystallised M3

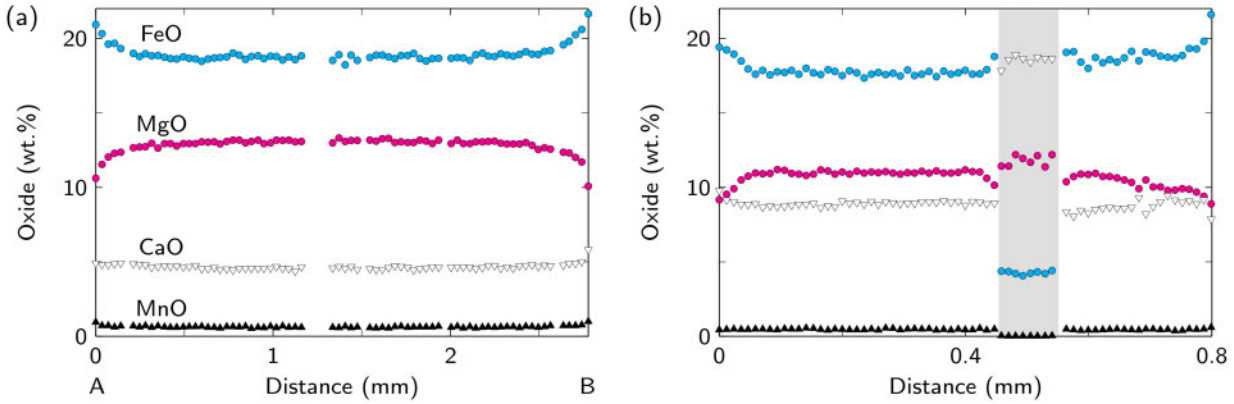

Figure 5: EMP line scans of selected element oxide concentrations across porphyroclastic M2 garnet. (a) Garnet with Type-C and -D inclusions in Lien garnet-websterite (DS1201). The position of the profile is shown in Figure 2c. (b) Garnet with Type-A inclusions in Aldalen eclogite (DS1425). The profile crosses a single omphacite lamella (shaded).

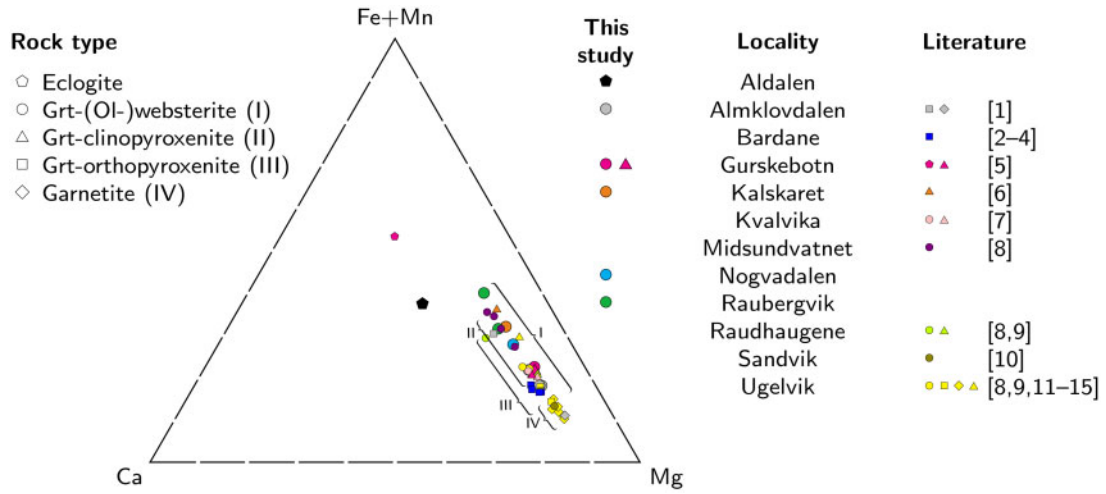

Figure 6: Triangular diagram showing relative proportions of divalent cations in non-recrystallised M2 garnet from WGR mantle pyroxenite, garnetite and eclogite. Braces labelled I–IV indicate the compositional variation of garnet from individual rock types. 1—Spengler *etal.* (2019), 2—van Roermund *etal.* (2002), 3—Carswell & van Roermund (2005), 4—Scambelluri *etal.* (2008), 5—Jamtveit (1984), 6—Jamtveit *etal.* (1991), 7—Apeiranthiti (2016), 8—Spengler *etal.* (2009), 9—Spengler (2006), 10—Lapen *etal.* (2005), 11—Spengler *etal.* (2006), 12—van Roermund *etal.* (2000b), 13—van Roermund *etal.* (2001), 14—Carswell (1973), 15—Carswell (1986).

clinopyroxene is, for small grains of 200 μm, generally homogeneous and similar to that of the rim of the porphyroclasts.

The eclogite contains M2 omphacite with an average composition of $Jd_{28}Aeg_4Di_{59}Hd_7En_1CaTs_1$ (Supplementary Data Electronic Appendix 2). The Mg# value is 0.842 and Ca# = Ca/(Ca+Mg) is 0.527. The Type-A lamellae in M2 garnet in this sample (Figures 3a–c and 5b) is omphacite as well but with a lower Na_2O content, $Jd_{23}Aeg_4Di_{62}Hd_8En_1CaTs_2$. Recrystallised M3 clinopyroxene with a grain size larger than 300 μm shows a core composition of $Jd_{28}Aeg_3Di_{57}Hd_8En_1CaTs_3$ and Na_2O and Al_2O_3 contents that decrease from core to rim (Supplementary Data Electronic Appendix 3). Mg# is 0.841 and Ca# is 0.533. The Cr_2O_3 content in all omphacite is low and varies little, 0.07–0.10 wt.%.

Clinopyroxene porphyroclasts in the pyroxenites are diopsidic in composition, $Jd_{2–15}Kos_{1–2}Di_{74–88}Hd_{3–12}En_{0–4}CaTs_{0–2}$ (Supplementary Data Electronic Appendix 2). Their Mg# values range from 0.865 to 0.950, Ca# is between 0.505 and 0.525 and the Cr_2O_3 content is moderate, 0.20–0.84 wt.%. Recrystallised grains with a minimum size of 300 μm are similar in endmember proportions, $Jd_{1–8}Kos_{1–3}Di_{75–90}Hd_{2–10}En_{0–4}CaTs_{1–3}$, Mg# number, 0.866–0.959, Ca# number, 0.504–0.517, and Cr_2O_3 content, 0.21–1.02 wt.% (Supplementary Data Electronic Appendix 3).

Orthopyroxene

Porphyroclastic M2 orthopyroxene is compositionally complexly zoned. Typically, the FeO content is homogeneous in crystal cores and increases slightly to noticeably at outermost crystal rims (Figure 9). The MgO content is inversely correlated with that of FeO. The variation of CaO and TiO_2 contents is very limited,

whereas that of Al_2O_3 shows two distinct patterns (Figure 9). From core to rim, the Al_2O_3 content can first decrease and then increase, which forms the shape of a 'W' (samples from Almklovdalen and Kalskaret; Figure 9a, c), or steadily increase resulting in the shape of a 'U' (samples from Gurskebotn and Raubergvik; Figure 9b, d). The core composition is Mg-rich ($En_{77–93}$) and low in CaO (0.10–0.27 wt.%), Al_2O_3 (0.44–0.67 wt.%) and Cr_2O_3 (0.03–0.09 wt.%; Supplementary Data Electronic Appendix 4).

Variable concentrations of Al_2O_3, CaO, MgO and FeO in recrystallised M3 orthopyroxene result in two patterns. Some grains show increasing Al_2O_3 from core to rim; the content of FeO is constant, like that of CaO, or increases at the outermost crystal rims (Figure 10a, b). MgO and FeO are inversely correlated. Such grains occur in pyroxenites with M2 orthopyroxene showing W-shaped Al_2O_3 profiles (Almklovdalen; Figure 9a, c) or lack M2 orthopyroxene (Nogvadalen). Samples with U-shaped Al_2O_3 profiles in M2 orthopyroxene (Gurskebotn, Raubergvik; Figure 9b, d) contain recrystallised grains with decreasing Al_2O_3 content from core to rim (Figure 10c, d). Contents of CaO either follow this trend or are constant, like those of MgO and FeO. M3 grain cores are also Mg-rich ($En_{75–93}$) and have low contents of CaO (0.07–0.29 wt.%) and Cr_2O_3 (<0.03–0.12 wt.%; Supplementary Data Electronic Appendix 5). The Al_2O_3 content in M3 orthopyroxene cores is lowest (0.18–0.23 wt.%) in samples with W-shaped Al_2O_3 profiles in M2 grains. An exception is sample DS0466 (Kalskaret) with high Al_2O_3 (1.12 wt.%) in M3 orthopyroxene showing the smallest M3 grain size (120 μm maximum) of the samples studied. Other samples have M3 orthopyroxene with intermediate to high Al_2O_3 (0.65–1.16 wt.%) in the cores. This content is similar to the composition of the M2 rims (Figure 9).

Olivine

Olivine in the pyroxenites is Mg-rich ($Fo_{88–91}$) and chemically homogeneous. Compositional differences between M2 and M3 olivine within each olivine-bearing sample were not detected at the analytical conditions chosen (Supplementary Data Electronic Appendix 6).

Amphibole

Grains of amphibole are compositionally zoned. The FeO and Al_2O_3 contents increase and the MgO content decreases from crystal core to rim. The composition of amphibole depends on the minerals being replaced. In eclogite, amphibole is less magnesian (Mg# 0.77) and chromian (0.06 wt.% Cr_2O_3), but richer in Na_2O (3.96 wt.%) than in the pyroxenites (0.82–0.92, 0.49–0.81 wt.% and 1.85–3.36 wt.%, respectively). Application of the nomenclature of Hawthorne *et al.* (2012) classifies the average compositions of analysed amphibole cores from all localities except Raubergvik (DS1201: actinolite, DS1225: magnesio-hornblende) as pargasite (Supplementary Data Electronic Appendix 7).

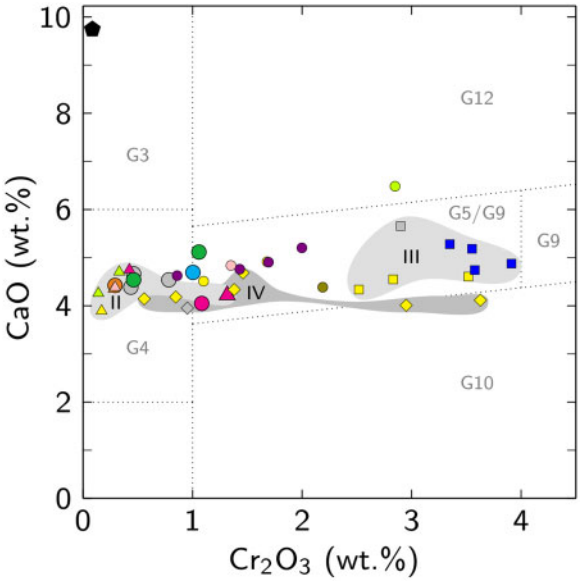

Figure 7: CaO vs. Cr_2O_3 (in wt.%) variation diagram for non-recrystallised M2 garnet from WGR mantle pyroxenite, garnetite and eclogite (legend as in Figure 6). Shaded fields labelled II–IV outline the compositional variation of garnet from selected rock types. Non-shaded fields refer to the classification of mantle-derived garnet of Grütter *et al.* (2004).

THERMOBAROMETRY

Applied geothermobarometry

Two different geothermometers and two different geobarometers were applied on average mineral core compositions of garnet, clinopyroxene and orthopyroxene (Supplementary Data Electronic Appendices 1–5). The thermometers and barometers were combined to iteratively estimate *P–T* conditions on a single mineral pair. By using two different mineral pairs of the same generation (M2 clinopyroxene–garnet and M2 orthopyroxene–garnet), the *P–T* conditions were estimated twice for generation M2. The same procedure was applied to mineral generation M3. Following this approach, it is possible to check the reproducibility of the calculated *P–T* conditions. The results are shown in Table 3 and Figures 11–13.

The garnet–clinopyroxene Fe^{2+}–Mg exchange thermometer calibration of Nakamura (2009) is based on graphite-buffered experimental partition data (to avoid issues related to uncertainties in the Fe^{3+} content) obtained in the *T* range of 800–1820 °C. The calibration includes thermodynamic data for the *P* dependency of the exchange reaction. The calculated *T* describes the experimental *T* used for the calibration with an uncertainty of ±74 °C (1σ). This thermometer was combined with the calibration for the ^{IV}Al-in-clinopyroxene–garnet barometer by Beyer *et al.* (2015). The barometer was calibrated using experimental data sets obtained from basaltic compositions in the *P–T* range of 2–7 GPa and 900–1550 °C. Its uncertainty is ±0.2 GPa (1σ). Due to the use of a thermodynamically consistent model for the

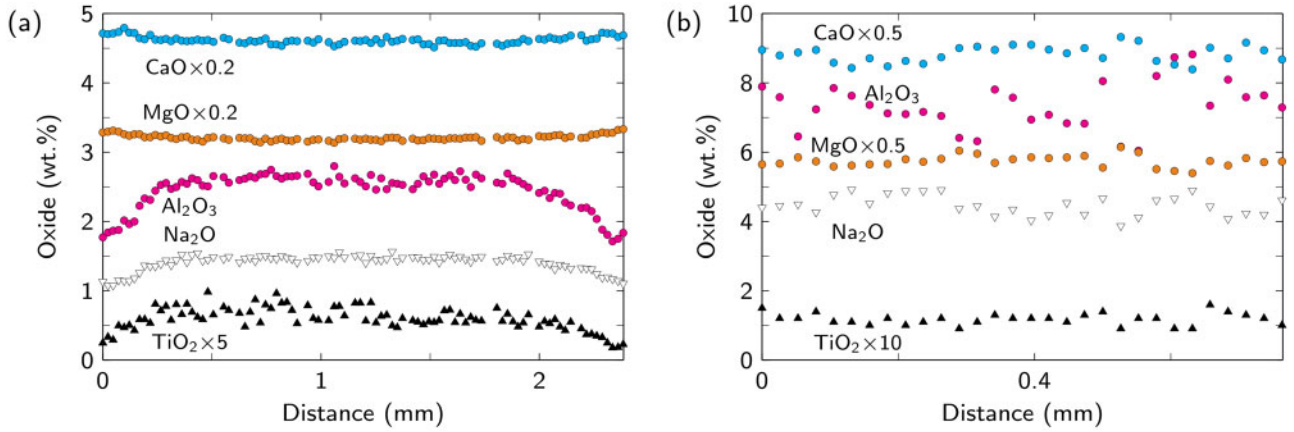

Figure 8: EMP line scans of selected element oxide concentrations across porphyroclastic M2 clinopyroxene. (a) Lien garnet-websterite (DS0318). (b) Aldalen eclogite (DS1425).

barometer calibration, their authors suggest its applicability down to 700 °C.

The Ca-in-orthopyroxene–clinopyroxene thermometer and the Al-in-orthopyroxene–garnet barometer, calibrated by Brey & Köhler (1990), were combined. Both calibrations are based on experimental data on low-Cr primitive natural lherzolitic compositions in the *P*–*T* range of 2.8–6.0 GPa and 900–1400 °C. The uncertainties (1σ) are ±0.22 GPa and ±19 °C.

Porphyroclastic M2 grains

The *P*–*T* estimates from porphyroclastic orthopyroxene–garnet pairs yielded two tight clusters (grey-shaded in Figure 11b). Three samples from Almklovdalen show a range in *P* of 2.86–3.06 GPa (average 3.00 GPa) and *T* of 705–710 °C (707 °C). The five samples from the Gurskbotn, Kalskaret and Raubergvik bodies record higher metamorphic *P* of 3.38–3.95 GPa (3.65 GPa) and *T* of 796–873 °C (841 °C).

Porphyroclastic clinopyroxene–garnet pairs provide similar information, although less clear (grey-shaded in Figure 11a). Three Almklovdalen samples form a tight *P*–*T* cluster at 2.8–3.1 GPa (2.93 GPa) and 720–760 °C (733 °C). Calculated values for the other samples are bimodal. The estimates from Aldalen, Kalskaret and Gurskebotn are at higher *P*–*T* conditions than those from Almklovdalen: 3.6–4.3 GPa (3.85 GPa) and 840–980 °C (885 °C). The Nogvadalen and Raubergvik samples yielded similar *P* of 3.9–4.2 GPa (4.07 GPa) but at lower *T* of 680–760 °C (730 °C).

Recrystallised M3 grains

The *P*–*T* conditions obtained from recrystallised orthopyroxene–garnet pairs show a twofold pattern (red-outlined and blue-shaded in Figure 11b). Determined *P* values are either higher or lower compared to those from M2 orthopyroxene for a specific sample. The high *P* estimates result from samples with low-Al orthopyroxene, which are from Almklovdalen (3.92–4.38 GPa, average 4.21 GPa; 675–707 °C, average 696 °C) and Nogvadalen (average: 5.16 GPa and 826 °C). *P*–*T* estimates from Gurskebotn, Kalskaret and Raubergvik form a cluster at low *P* with ranges of 1.96–2.79 GPa (2.29 GPa) and 714–834 °C (771 °C).

Thermobarometry on recrystallised clinopyroxene–garnet pairs shows an alike twofold *P*-sensitive pattern (red-outlined and blue-shaded in Figure 11a). The Almklovdalen samples gave *P*–*T* estimates at high *P*. Two samples are similar with an average at 4.15 GPa and 700 °C, whereas the other estimate for this body yielded higher values of 5.4 GPa and 780 °C. Likewise, the Nogvadalen sample resulted in high *P*–*T* estimates. M3 clinopyroxene paired with M2 garnet suggests 4.8 GPa and 710 °C, whereas M3 clinopyroxene paired with M3 garnet indicates much higher values of 6.2 GPa and 870 °C. The seven estimates from the other samples (Aldalen, Gurskebotn, Kalskaret and Raubergvik) form a large but homogeneous cluster at low *P* with ranges of 1.9–2.9 GPa (2.39 GPa) and 680–810 °C (729 °C).

DISCUSSION

Sequence of microstructure formation

Type-A to -F microstructures (Table 2) occur solely in pre-Scandian M2 garnet. Therefore, the variable microstructural record among the studied sample locations can in part be explained by a variable degree of preservation during Scandian recrystallisation and alteration. Several observations argue the microstructures to have formed in a row. For example, the planar structures in garnet (Figure 3n–q) typify a relatively late origin for theType-F inclusions, but before the dynamic recrystallisation. Uniformly distributed inclusions (Type-A to -D) formed early in the rock history because they occur in extended garnet core areas cut by Type-F inclusions. In contrast, Type-E inclusions seem to be related to the Scandian dynamic recrystallisation, because they were found only in the most intensely recrystallised sample. This suggests the following sequence of origin: Type-A to -D were followed by Type-F and latest by Type-E.

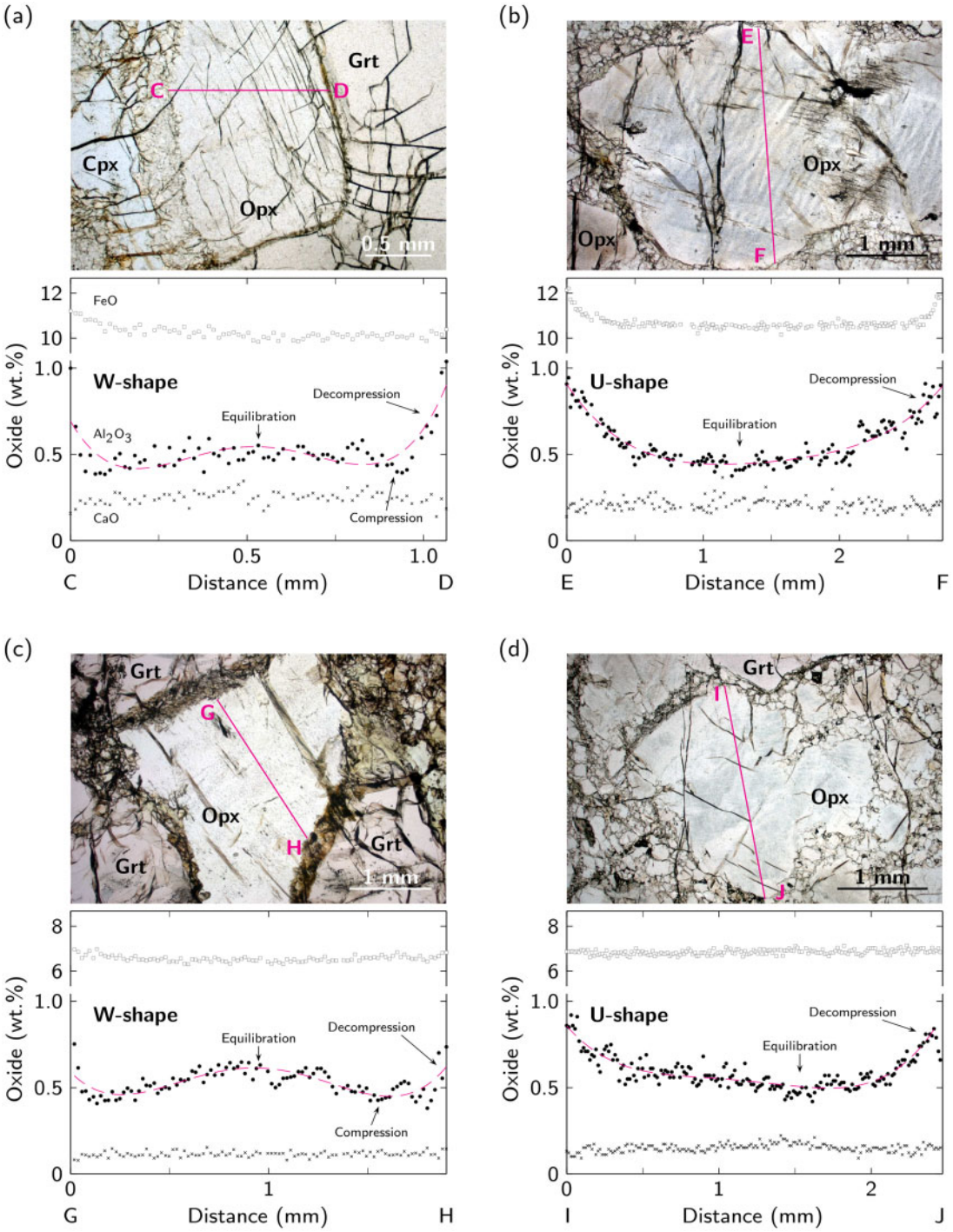

Figure 9: EMP line scans across porphyroclastic M2 orthopyroxene (solid lines in the plane-polarised light images) showing Al_2O_3 (•), CaO (×) and FeO (□) concentrations. The data were fitted to a 4th order polynomial (dashed lines). Note W- and U-shaped forms. Labels refer to the interpretation of characteristic sections. (a) Kalskaret garnet-websterite (DS0466). (b) Raubergvik garnet-websterite (DS1225). (c) Lien garnet-websterite (DS0318). (d) Gurskebotn garnet-websterite (DS1249).

Systematic variation of uniformly distributed inclusions

Samples from each studied location show Type-C and -D inclusions and most of them additionally have other types of inclusions with uniform distribution (Table 2). This suggests that all samples and thus all studied peridotite bodies share a common history that includes the formation of oriented lamellar inclusions in garnet. This suggestion is in agreement with similar microstructures of silicate and oxide inclusions in M2 garnet preserved in other WGR peridotite bodies (van Roermund & Drury, 1998; van Roermund *et al.*, 2000a,

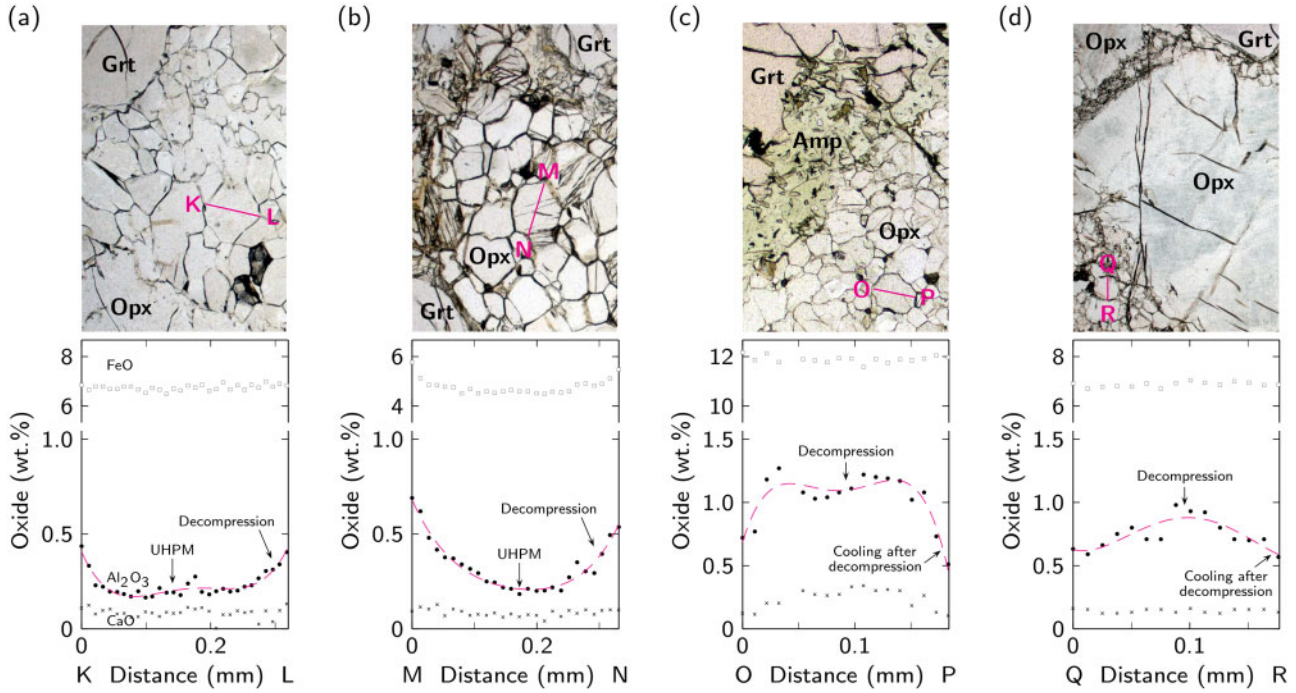

Figure 10: EMP line scans across recrystallised M3 orthopyroxene (solid lines in the plane-polarised light images) showing Al_2O_3 (•), CaO (×) and FeO (□) concentrations. The data were fitted to a 4th order polynomial (dashed lines). Labels refer to the interpretation of characteristic sections. (a) Lien garnet-websterite (DS0318). (b) Rødhaugen garnet-websterite (DS1245). (c) Raubergvik garnet-websterite (DS1225). (d) Gurskebotn garnet-websterite (DS1249).

2017; Hwang *et al.*, 2013). It follows from the microstructual systematics that most if not all WGR garnet-peridotite bodies share a long history, which includes the microstructural evolution of different types of pyroxenite, garnetite and some mantle eclogite. Perhaps, this microstructural evolution includes a shared origin for all these mantle rock types. An indication for this assumption is the major element chemistry of garnet in these rocks that defines a narrow chemical trend that overlaps for different rock types and is independent of sample location (Figures 6 and 7).

All inclusion types with uniform distribution (Type-A to -D) are genetically related, because they show the following common features: (1) the larger inclusions (Type-A to -C) generally have long aspect ratios and inferred preferred orientation in garnet (Figure 3a–m, q), (2) the inclusion size (thickness) correlates with the inclusion spacing (Figure 3b, c, g–i), (3) small inclusions fill the space between larger inclusions in support of consecutive generations (Figure 3c, g–i), (4) the mineral phases of the inclusions change systematically with their inclusion size: the largest (Type-A) consists solely of pyroxene, the second largest (Type-B) is dominated by pyroxene and rarely has Ti-oxides, whereas the smaller ones (Type-C and -D) are characterised by subordinate pyroxene and dominant Ti-oxides (Figure 3h–m), (5) inclusions disappear in sequence to smaller ones at garnet rims (Figure 3k). These microstructural features suggest that these inclusions were formed progressively by the same process.

Several mechanisms were proposed to explain the formation of acicular oriented inclusions of pyroxene and/or rutile in garnet. They include: (1) solid-state exsolution from majoritic and titaniferous garnet in a chemically closed system (Haggerty & Sautter, 1990; Ague & Eckert, 2012; Spengler & Alifirova, 2019), (2) solid-state open-system precipitation that requires transfer of oxygen and/or cations by volume diffusion between the matrix and the garnet interior (Proyer *et al.*, 2013; Keller & Ague, 2020), (3) cleaving and healing of garnet with rutile crystallisation in a fluid- or melt-bearing environment (Hwang *et al.*, 2007), (4) metasomatic dissolution-reprecipitation (Hwang *et al.*, 2019), (5) co-precipitation during garnet growth (Hwang *et al.*, 2015; Griffiths *et al.*, 2020). The mechanism that caused the uniform distribution of oriented pyroxene and rutile lamellae in our garnets must explain the formation of different inclusion sizes including the correlation with different inclusion spacings, i.e. up to four inclusion generations. Such a sequence of inclusions has not been reported in publications that proposed mechanisms (2), (3), (4) or (5) as they result in the formation of only one generation of oriented inclusions in garnet. Several generations of oriented lamellae are well documented from mineral solid-solution systems that underwent exsolution by mechanism (1), e.g. in the pyroxene–garnet (Sautter & Harte, 1988; Sautter & Fabriès, 1990) and ilmenite–hematite systems (McEnroe *et al.*, 2007). These sets of inclusions show thicker

Table 3: Thermobarometric estimates using mineral compositions in Supplementary Data Electronic Appendices 1–5 (*P* in GPa/*T* in °C).

Locality	Aldalen	Almklovdalen			Gurskebotn		Kalskaret	Nogvadalen	Raubergvik	
		Lien	Rødhaugen							
Sample	DS1425	DS0318	DS1245	DS1246	DS1249	DS1252	DS0466	AH0364	DS1201	DS1225
(1) M2 Cpx–M2 Grt, Beyer et al. (2015)/Nakamura (2009)										
	3.6/860	3.1/720	2.8/720	2.9/760	3.6/840	4.3/980	3.9/860	4.1/680	3.9/760	4.2/750
(2) M3 Cpx–M2 Grt, Beyer et al. (2015)/Nakamura (2009)										
	2.5/810	4.2/700	4.1/700	5.4/780	2.2/680	2.9/740	2.4/750	4.8/710	1.9/680	2.9/680
(3) M3 Cpx–M3 Grt, Beyer et al. (2015)/Nakamura (2009)										
	1.9/760	–	–	–	–	–	–	6.2/870	–	–
(4) M2 Opx–M2 Grt, Brey & Köhler (1990)										
	–	2.86/705	3.09/705	3.06/710	3.56/796	3.68/873	3.70/845	–	3.38/854	3.95/836
(5) M3 Opx–M2 Grt, Brey & Köhler (1990)										
	–	4.34/706	4.38/707	3.92/675	2.20/714	2.79/746	2.17/769	5.13/825	1.96/790	2.35/834
(6) M3 Opx–M3 Grt, Brey & Köhler (1990)										
	–	–	–	–	–	–	–	5.20/828	–	–

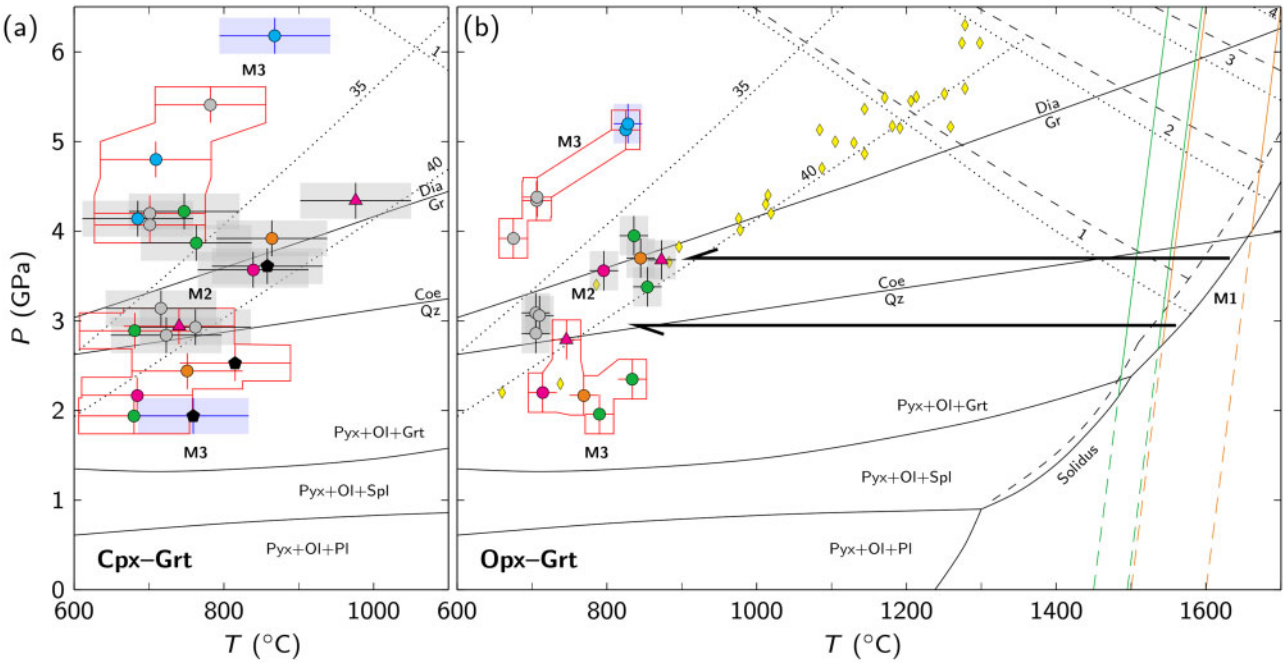

Figure 11: Phase diagrams (CMAS system; solid curves; Gasparik, 2000) with thermobarometric estimates (Table 3) on (a) clinopyroxene–garnet and (b) orthopyroxene–garnet pairs. Large symbols are the same as in Figure 6. Small diamonds, W Greenland SCLM xenoliths (values and references are given in Supplementary Data Electronic Appendix 8). Solid lines emanating from the symbols depict uncertainties (1σ) of the thermobarometers. Shadings and outlines of uncertainty ranges refer to combinations of mineral generations: porphyroclastic M2 grains (grey), porphyroclastic M2 garnet & recrystallised M3 pyroxene (red), recrystallised M3 grains (blue). Labelled long lines show the phase transitions for graphite–diamond (Day, 2012) and quartz–coesite (Klein & Hurlbut, 1993). Dotted lines labelled 35 and 40 show continental conductive geotherms (numbers refer to mW m^{-2} surface heat flow; Hasterok & Chapman, 2011). Lines labelled 1 to 4 are isopleths for $^{VI}Si \times 100$ in garnet representing pyroxene (mol%) in solid-solution with garnet for CMAS (dotted) and NCMAS (dashed, including solidus; Gasparik, 2014). Green and brown lines enclose ranges for adiabats of Archaean ambient mantle (2.5–3.4 GPa) deduced from T_p minima of Ganne & Feng (2017) and T_p of Herzberg *et al.* (2010), respectively, and an adiabatic gradient of 0.5 °C km^{-1} (Katsura *et al.*, 2010). Arrows depict the proposed early evolution of samples from the Aldalen, Almklovdalen, Gurskebotn, Kalskaret and Raubergvik bodies. Other labels refer to different mineral generations based on mineral texture and microstructure (M1—unexsolved grains, M2—exsolved grains, M3—dynamically recrystallised grains).

lamellae to have formed at higher *T* than thinner lamellae. Therefore, the formation of Type-A to -D inclusions in our pyroxenite and eclogite samples is more in line by exsolution of consecutive mineral generations whose inclusion size is a *T* indicator. This reasoning corroborates earlier interpretations on the origin of oriented lamellar pyroxene in mantle garnet of the WGR (van Roermund & Drury, 1998).

Nucleation and growth of pyroxene (Type-A and -B) can be explained by reactions that involve a majorite

component ($M_4Si_4O_{12}$) in a solid-solution of garnet (Ringwood, 1967):

$$M_3[AlM_{0.5}Si_{0.5}]Si_3O_{12} \rightarrow M_2Si_2O_6 + 0.5\,M_3Al_2Si_3O_{12} \quad (1)$$

and a Na-majorite component ($Na_2MgSi_5O_{12}$) in a solid-solution of garnet (Sobolev & Lavrent'ev, 1971):

$$NaM_2[AlSi]Si_3O_{12} \rightarrow M_2Si_2O_6 + NaAlSi_2O_6 \quad (2)$$

with M = Mg^{2+}, Fe^{2+} and Ca^{2+}. The crystallisation of Ti-oxides together with pyroxene (Type-B, -C and -D) points to Ti in the garnet lattice probably as Ti^{4+} (Grew *et al.*, 2013), in both octahedral and tetrahedral sites (Locock *et al.*, 1995; Ackerson *et al.*, 2017a). According to charge balance constraints, $^{VI}Ti^{4+}$ requires a coupled substitution with either a divalent ion $^{VI}M^{2+}$ in the octahedral site (morimotoite substitution; Henmi *et al.*, 1995), or a trivalent ion $^{IV}(Fe, Al)^{3+}$ in the tetrahedral site (schorlomite and hutcheonite substitutions; Ito & Frondel, 1967; Ma & Krot, 2014), or the half of $^{IV}(2H)^{2+}$ in the tetrahedral site (Ti-hydrogarnet substitution; Reynes *et al.*, 2020), or a monovalent ion, such as $^{VIII}Na^{+}$, or perhaps half a vacancy ($^{VIII}\square_{0.5}$) in the dodecahedral site (Bishop *et al.*, 1976; Yang & Liu, 2004). In contrast, substitution of Si by $^{IV}Ti^{4+}$ does not require charge balance. When considering these substitutions for Ti in garnet, the syngenetic exsolution of Ti-oxides (rutile, ilmenite) and pyroxene (Figure 3h, i, l, m) from a hypothetical titaniferous majorite component in mantle garnet can be explained by the following reactions:

$$M_2\square Ti_2(TiSi_2)O_{12} \rightarrow 3\,TiO_2 + M_2Si_2O_6 \quad (3)$$

$$M_3[MTi](TiSi_2)O_{12} \rightarrow 2\,MTiO_3 + M_2Si_2O_6 \quad (4)$$

$$M_3[MTi]Si_3O_{12} \rightarrow MTiO_3 + 1.5\,M_2Si_2O_6 \quad (5)$$

$$M_3[TiAl](AlSi_2)O_{12} + M_3Ti_2(H_2Si_2)O_{12} \rightarrow 2\,MTiO_3 + TiO_2 + 0.5\,M_2Si_2O_6 + M_3Al_2Si_3O_{12} + H_2O \quad (6)$$

The garnet components in equations (3) and (4) contain Ti in the octahedral and tetrahedral positions of the garnet structure. This is in consensus with natural and experimental data that show that $^{IV}Ti^{4+}$ occurs only in garnet with insufficient Fe^{3+} to occupy only tetrahedral sites (Dowty, 1971; Povarennykh & Shabalin, 1983). Equations (3) and (4), if combined in suitable proportion, can form rutile and ilmenite in any ratio. The other two equations (5) and (6) have garnet components that contain Ti solely in octahedral coordination. Ilmenite is the prevalent Ti-oxide being formed by these equations. When considering the strong predominance of rutile over ilmenite of Type-C and -D (Table 2, Figure 3), then equations (3–6) imply that most rutile crystallised from Ti-bearing garnet that had a partial vacancy in the garnet structure. Such vacancies were proposed for Ti-bearing garnet by theoretical considerations (Yang & Liu, 2004; Smith, 2006; Proyer *et al.*, 2013), but are not supported by available experimental studies (Kawasaki & Motoyoshi, 2016; Ackerson *et al.*, 2017b). These experiments were carried out in the ranges for *P* of 0.7–2.5 GPa and *T* of 800–1300 °C on garnet compositions that were rich in almandine component (37–66 mol%). Lamellar microstructure-bearing SCLM garnet differs in that it formed at higher *P* (Figure 12) and higher *T* (Carswell, 1973; Spengler & Alifirova, 2019) and has pyrope-rich compositions (Figure 6). Hence, whether or not vacancy-bearing substitutions may occur in SCLM garnet remains unknown.

Although all types of inclusions with uniform distribution can be explained by the above-mentioned reactions, the nucleation and growth of solely rutile during the compositional change of the titaniferous garnet host may be considered for stoichiometric reasons. Such a reaction can, for instance, be formulated by allowing some Ti to occupy the dodecahedral site ($^{VIII}Ti^{4+}$):

$$1.5\,M_2\square_{0.66}Ti_{0.33}[Ti_{0.66}Al_{1.33}](TiSi_2)O_{12} \rightarrow 3\,TiO_2 + M_3Al_2Si_3O_{12} \quad (7)$$

The ionic radius of Ti^{4+} in eightfold coordination (0.74 Å; Shannon, 1976) is 17 % smaller than that of Mg^{2+} (0.89 Å). This implies that a high vibrational state (high *T*) and high *P* favour Ti^{4+} to enter the dodecahedral site in pyropic garnet. A decreasing pyrope content along the pyrope–grossular and pyrope–almandine binary joins increases the volume of the unit cell and that of the dodecahedral site (Ganguly *et al.*, 1993; Kuang *et al.*, 2019), which may cause $^{VIII}Ti^{4+}$ to become energetically less favourable. Synchronously with a unit cell increase increases (to a lesser degree) the volume of the octahedral site. Magnified octahedral sites may favour ions larger than $^{VI}Al^{3+}$ (0.535 Å) to enter, which is consistent with an observed increase of the $^{VI}Ti^{4+}$ (0.605 Å) solubility with increasing grossular content (Ackerson *et al.*, 2017a). Thus, solubility, site occupancy and substitution mechanisms of Ti in garnet are complexly interdependent and sensitive to several parameters including *P*, *T* and mineral chemistry. As noted before, however, studies on experimental and natural garnet have shown that Ti^{4+} substitutes cations in four- and sixfold coordination, whereas eightfold coordinated Ti^{4+} has not been detected (Kawasaki & Motoyoshi, 2016; Ackerson *et al.*, 2017b). Possible reasons for the lack of evidence for $^{VIII}Ti^{4+}$ in these garnets may include that (1) the synthetic garnet chemistry did not exceed a pyrope component of 50 %, (2) the natural pyrope-rich garnet was too low in Ti content and (3) the experimental *P*–*T* conditions were not suitable for the study of garnet that originated in the SCLM.

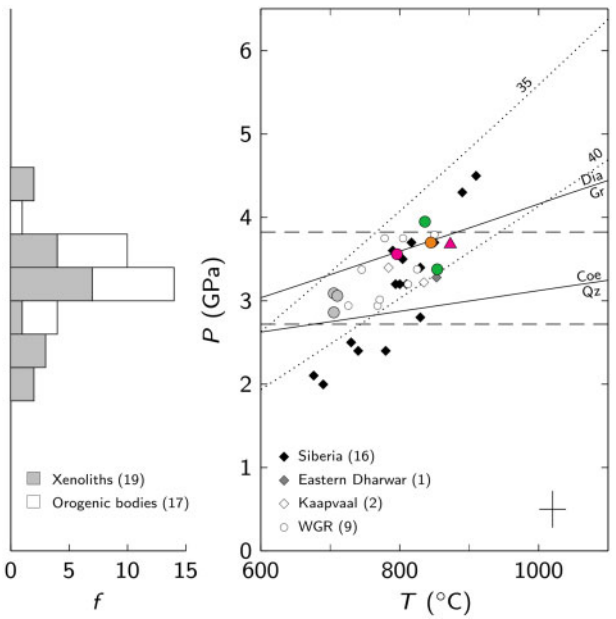

Figure 12: *P–T* diagram (right) and *P* frequency distribution (left) of global SCLM samples that contain garnet with oriented lamellar inclusions (pyroxene and/or Ti-oxides) and cofacial orthopyroxene, subdivided by type and provenance. Numbers in brackets refer to sample counts. All *P–T* data base on the Ca- and Al-in-orthopyroxene thermobarometer calibrations of Brey & Köhler (1990) and were partially recalculated (values and references are given in Supplementary Data Electronic Appendix 8). The cross refers to the uncertainties (1σ) of the thermobarometer calibrations. Dashed lines delineate the mean *P* confidence interval of the data set shown (1σ, n = 36). Other lines and symbols are the same as in Figure 11.

Independent support for a possible structural vacancy in former titaniferous SCLM garnet is provided by experimental studies on an analogue, the Ca-Eskola ($Ca_{0.5}\square_{0.5}AlSi_2O_6$) component in eclogitic omphacite (Konzett *et al.*, 2008; Schroeder-Frerkes *et al.*, 2016). This vacancy-bearing component also requires SCLM *P* to form and is maximised at near solidus *T*. Similar to $^{VIII}Ti^{4+}$ in equation (7), the ionic radius of Al^{3+} in sixfold coordination (0.535 Å) is 40 % smaller than that of Mg^{2+} in the same coordination (0.89 Å). Nevertheless, the experimental data show that high metamorphic conditions and especially high *T* conditions allow Al^{3+} to enter the octahedral site in omphacite. Likewise, the breakdown of this vacancy-bearing component is regarded to form SiO_2 rods with shape preferred orientation in omphacite by exsolution (Katayama *et al.*, 2000; Zhang *et al.*, 2005) after the reaction:

$$2\ Ca_{0.5}\square_{0.5}AlSi_2O_6 \rightarrow 3\ SiO_2 + CaAl_2SiO_6 \qquad (8)$$

Whilst Ti^{4+} substitution at dodecahedral positions in garnet has not been demonstrated, reaction (7) may be regarded as hypothetical. Alternatively, the possibility for the crystallisation of solely rutile from sixfold coordinated Ti^{4+} in garnet has been proposed to be associated with an oxidation of Fe^{2+} to Fe^{3+} (Proyer *et al.*, 2013) by the reaction:

$$6\ M_3[TiAl](AlSi_2)O_{12} + 6\ M_{2.5}\square_{0.5}[TiAl]Si_3O_{12} \rightarrow 10\ M_3[Al_{1.8}Fe^{3+}{}_{0.2}]Si_3O_{12} + M^{2+} + 2\ e^- + 12\ TiO_2 \qquad (9)$$

Application of equation (9) to the origin of Type-C and -D inclusions implies that rutile exsolution was triggered chemically by a change in the redox state of the SCLM garnet during its early evolution. Such a scenario has to explain the geometric features of the microstructure with uniform distribution, e.g. the correlation between inclusion size and spacing, the sequential disappearance of inclusion types at garnet margins and the co-crystallisation of pyroxene and rutile that partially form single rods (Figure 3). However, a single chemical process alone seems unlikely be able to explain the formation of rutile in successive stages that have their own microstructural characteristics. These two rutile generations, their specific microstructures and the *T* dependency of the Ti solubility in garnet, taken together, favour that rutile crystallisation was triggered physically by cooling. Perhaps, this cooling event was accompanied by an oxidation event that affected the SCLM garnet sequentially at two different *T*'s and thus would add complexity to its evolution. In this maybe unlikely case, reaction (9) may explain the formation of solely rutile of Type-C and -D provided that each partial oxidation allowed for the removal of divalent cations from the garnet host.

Overprint on the primary microstructure

Type-F inclusions differ in many regards to Type-A to -D discussed above. Most obvious is the diversity of minerals and fluid involved, the alignment of the inclusions along planar structures and the cutting relationships with Type-C and -D inclusions (Figure 3p, q). This suggests that the mechanism and the timing of formation of Type-F inclusions differ fundamentally to those of Type-A to -D. A large proportion of the Type-F inclusions includes mobile components (H, C, N) as evident from carbonates, hydrous minerals and fluid inclusions (Figure 4) suggesting an origin related to an infiltrating fluid. This fluid seems to have migrated along subparallel and subcurvaceous planes in garnet (Figure 3n, o). We interpret these planar structures as cracks, in which crystals nucleated and grew from the fluid. In addition, a part of the migrating fluid was trapped as fluid inclusion while the crack healed. A halo of depletion of Type-D inclusions proximal to the healed cracks (Figure 3p) may evince that the healed crack inclusions postdate Type-D inclusions and furthermore that preexisting inclusions were leached in the host garnet and likely became part of Type-F precipitates. If true, this demonstrates that infiltrating fluids obliterated rutile inclusions in garnet.

The original grain boundary area of M2 garnet is free of Type-F inclusions (Figure 3n). This suggests that the

fluid infiltration stage was followed by an annealing stage that affected the garnet grain boundaries. Therefore, the fluid overprint might predate the Scandian recrystallisation and UHP metamorphism, and thus occurred while the mantle fragments resided in the SCLM of E Greenland. As a result, the entrapped fluids demonstrate hydration of SCLM that overlayed a subduction zone most likely by means of subduction zone fluids.

Deformation (cf. curved outline of Type-A lamella in Figure 3b) and alteration (Figure 3e) clearly overprinted some inclusions. The sample with the most intense recrystallisation contains rutile inclusions (Type-E), which appear to be associated with dislocations in the garnet host. Similar rutile inclusions along dislocations have been reported from protogranular and porphyroclastic garnet of the Ugelvik and Raudhaugene bodies (van Roermund *et al.*, 2000a). Dislocations are known to form in response to deformation. Therefore these rutile grains seem to have resulted from deformation, perhaps by precipitate dragging along migrating dislocations (Nes & Solberg, 1973). If this mechanism applies, then the Type-E inclusions may represent strain-induced redistributed Type-D inclusions.

Position and evolution in the SCLM

Rock texture, garnet microstructure and thermobarometry suggest that all samples share three evolutionary processes: an exsolution of solid-solution precursor minerals (M1), followed by a mineral-chemical equilibration in the SCLM (M2) and a subsequent dynamic recrystallisation (M3).

The M2 mineral chemistry constrains the residence position of the samples in the SCLM provided that the effect of post-M2 element diffusion on M2 *P–T* determinations can be assessed. This is of importance, because the diffusivity of elements used in the thermobarometers increases in pyroxene in the order $Al^{3+} < Ca^{2+} < Mg^{2+}$, Fe^{2+} (Cherniak & Dimanov, 2010; Jollands *et al.*, 2016), which may generate complex element concentration gradients in M2 grains during UHP metamorphism and retrogression. The effect of diffusion on the M2 mineral chemistry is discussed in context with the M3 metamorphic evolution further below.

Several observations suggest that most M2 mineral core compositions represent equilibrium: (1) M2 thermobarometric estimates on different samples form clusters, (2) these clusters largely overlap for the M2 mineral pairs orthopyroxene–garnet and clinopyroxene–garnet, (3) the calculated *P–T* conditions are body-specific (i.e. low for Almklovdalen and high for Aldalen, Gurskebotn, Kalskaret and Raubergvik) and (4) the *P–T* clusters coincide with a steady-state mantle geotherm (Figure 11). *P–T* estimates on M2 clinopyroxene–garnet pairs from two bodies (Nogvadalen and Raubergvik) deviate from the clusters. This deviation probably relates to chemical disequilibrium between the two M2 minerals possibly due to an effective grain size reduction in

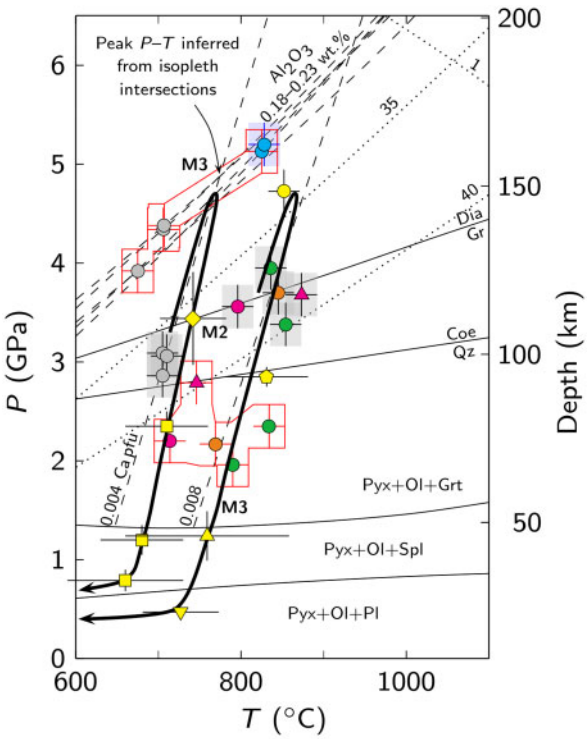

Literature data (sample locations are shown in Figure 1):

Stadlandet–Nordfjord area

- Average (n=16) UHP Opx-eclogite, Cuthbert *et al.* (2000), error bars are 1σ of the data set
- Gneiss NF42, Krokkenakken, McDonald *et al.* (2018), error bars refer to 1σ (thermobarometry) or isopleth ranges in pseudosections

Gurskøy–Storfjord area

- Grt-websterite QC29A, N Remøy, Quas-Cohen (2014), average of 2 mineral pairs (Opx Al_2O_3 0.27–0.29 wt.%) recalculated using the Ca- and Al-in-Opx calibrations of Brey & Köhler (1990), error bars are 1σ (thermobarometry)
- Opx-eclogite 9814i4, N of Stranda, Walsh & Hacker (2004), error bars are 1σ (thermobarometry)
- Average (n=4) metapelite, Root *et al.* (2005), error bars are 1σ of the data set
- Metapelite R9828C30, Sandsøya, Root *et al.* (2005), error bars are 1σ (thermobarometry)

Figure 13: *P–T* diagram showing the metamorphic evolution proposed for mantle samples exposed in different areas (Stadlandet–Nordfjord, Gurskøy–Storfjord). Dashed lines are selected isopleths for Ca in M2 orthopyroxene and Al_2O_3 in M3 orthopyroxene. Their intersections are used to infer area-specific peak metamorphic conditions. Different types of crustal rocks define retrograde paths (arrows) subparallel to the Ca isopleths. Other symbols, compositional fields and lines as in Figure 11. *P* to depth conversion is from Anderson (1989).

these samples (Figure 2c, d). By disregarding these three *P–T* pairs from Nogvadalen and Raubergvik and by giving greater weight to the *P–T* estimates based on M2 orthopyroxene (due to low Al^{3+} and Ca^{2+} diffusivities in pyroxene) then the Almklovdalen body and the group of ultramafics from Aldalen, Gurskebotn, Kalskaret and Raubergvik equilibrated at 3.0 GPa and 710 °C and at 3.7 GPa and 840 °C, respectively. These equilibration conditions are similar to those of earlier

studies on M2 mineral assemblages from Almklovdalen (2.9 GPa and 730 °C; Spengler *et al.*, 2019) and from Kalskaret (3.5 GPa and 840 °C; Paquin, 2001). All these *P–T* estimates are within the stability field of coesite and at a cratonic geotherm related to 37–38 mW m^{-2} surface heat flow (Hasterok & Chapman, 2011; Figure 11). Thus, five of the six studied peridotite bodies resided at two discrete SCLM depth levels, which correspond to approximately 100 km and 120 km considering the Preliminary Reference Earth Model for the *P* to depth conversion (Anderson, 1989). Furthermore, our M2-based *P–T* estimates are in line with those from comparable mantle fragments that lack a tectonic overprint. For example (5), garnet-peridotite xenoliths from the North Atlantic craton and an adjacent area show that the Archaean SCLM in southern W Greenland was similarly cold during the late Neoproterozoic (corresponding to a geotherm of ~39 mW m^{-2} surface heat flow; Bizzarro & Stevenson, 2003; Sand *et al.*, 2009) as in central E Greenland during the Palaeozoic (this study) if the same thermobarometric calibrations are used (Figure 11b). Another example (6) concerns global SCLM garnet that contains oriented pyroxene and/or Ti-oxide lamellae (Figure 12). These samples equilibrated within a narrow depth range corresponding to 3.3 ± 0.6 GPa (1σ, n = 36; average of 19 xenolith samples: 3.2 ± 0.7 GPa; average of 17 orogenic samples: 3.4 ± 0.4 GPa) and have a frequency distribution that is virtually independent on the sample type (xenolithic, orogenic) if the same thermobarometric calibrations are used. For these six reasons we interpret our M2-based *P–T* estimates to be relevant.

Exsolved pyroxene and Ti-oxides imply that the M1 precursor garnets were enriched in Si and Ti. This enrichment has been shown to increase for each element with both *P* and *T*, e.g. for Si in garnet experimentally (Fei & Bertka, 1999) and thermodynamically (Collerson *et al.*, 2010; Gasparik, 2014) and for Ti in garnet experimentally (Kawasaki & Motoyoshi, 2016; Ackerson *et al.*, 2017b). These studies have also shown that the solubility for Si in garnet depends strongly on *P* and less on *T* but is the other way round for Ti. The chemical systems applied range from simple, like $MgO–Al_2O_3–SiO_2$ (MAS; Fei & Bertka, 1999), to more complex, like $Na_2O–CaO–MgO–FeO–Al_2O_3–SiO_2$ (NCMFAS; Collerson *et al.*, 2010), and natural systems (Kawasaki & Motoyoshi, 2016). Equally dependent on *P* and *T* should be the reverse process of exsolution. Useful criteria to distinguish if decompression or cooling or both together formed the driving force for exsolution in natural garnet come from petrological observations on the host mineral assemblage. Websteritic M2 pyroxene associated with M2 garnet contains Ca-pyroxene lamellae in Mg-pyroxene and vice versa (Figure 3s), which indicates a cooling component. Similar microstructures, i.e. M2 garnet containing lamellar pyroxene associated with M2 orthopyroxene containing lamellae of Ca-pyroxene and an Al-phase, occur in comparable samples from the Almklovdalen, Bardane and Ugelvik bodies (Carswell & van Roermund, 2005; Spengler, 2006; Spengler *et al.*, 2019). Thermodynamic data in the CMAS and NCMAS systems (Gasparik, 2000, 2014) constrain syngenetic exsolution of pyroxene lamellae in both host minerals by either near isobaric or decompression assisted cooling. Decompression, however, increases the solubility of Al in pyroxene (Gasparik, 2014). Therefore, decompression is not a viable process to explain Al minerals to have exsolved from pyroxene coevally with pyroxene from garnet of the same mineral assemblage. In consequence, the M2 grains in Almklovdalen websterite have exsolved minerals formed by near isobaric cooling. The microstructural systematics of the sample suite implies that this cooling scenario befell all samples. It follows that the near isobaric cooling was accompanied with the successive exsolution of first only excess Si and then gradually of excess Ti once the *T* of Ti-saturation in garnet was reached. Otherwise Ti-oxide lamellae are to be expected not only of Type-C and -D but also of Type-A and -B. It follows further that a near isobaric extrapolation from the depth of sample equilibration in the SCLM (M2) to the *P–T* field of garnet with a significant pyroxene component in solid-solution (M1) allows to estimate an early *T* from where the sequential exsolution may have begun (arrows in Figure 11b).

Constraints on the formation of the Central E Greenland SCLM

The proposed near isobaric cooling trajectories intersect isopleths for circa 0.9–1.5 mol% (CMAS) and 0.8–1.2 mol% (NCMAS) pyroxene in garnet solid-solution (Gasparik, 2014), the dry peridotite solidus (Gudfinnsson & Presnall, 1996) and adiabats for Archaean ambient mantle—deduced from the potential *T* (T_p) of Herzberg *et al.* (2010) and Ganne & Feng (2017) in combination with an adiabatic gradient of 0.5 °C km^{-1} of Katsura *et al.* (2010) – in the *T* range of 1500–1600 °C (Figure 11b). The addition of Ti to the chemical systems applied likely influences slope and/or position of the garnet Si isopleths in *P–T* space. Though, Ti in garnet was below saturation at high *T* and formed a minor component like Na, whose effect on the Si isopleths is small (Figure 11b). Therefore, the influence of Ti onto garnet Si isopleths is presumably small too. In this case, the combination of mineral chemistry, mineral microstructure, petrology and thermodynamic data suggests the garnet-websterite and eclogite samples to have crystallised within 3.0–3.7 GPa and 1500–1600 °C. This *P–T* estimate is similar to the crystallisation conditions inferred from the whole-rock major element chemistry of another exsolution microstructure-bearing garnet-pyroxenite from Ugelvik (Figure 1; 3.5–4.0 GPa and 1500–1600 °C; Carswell, 1973).

If, in this *T* range of 1500–1600 °C, the pyroxenite and eclogite samples formed from melt that migrated through the dunitic host peridotites, then this melt must have been formed at depths greater than those where the samples equilibrated (i.e. greater 3.0–3.7 GPa). Any shallower depths would not have resulted in the

formation of the exsolution microstructure in garnet (Gasparik, 2014). Only the hottest adiabat for Archaean ambient mantle with a T_p of 1600 °C can cause minimal peridotite decompression melting at P beyond 3.7 GPa (Figure 11b). Therefore, the origin of the sampled rocks is unlikely related to peridotite melting in an Archaean mid-ocean ridge setting. Alternatively, if recycled ocean floor was the source of the melt within rising upper mantle, then this melt should be in disequilibrium with the embedding peridotite and would react with it to form pyroxenite (Sobolev *et al.*, 2005). In this case, the host dunite is necessarily also recycled mantle to allow for its major melt extraction prior to the pyroxenite origin. However, this is not evident from whole-rock isotope model ages and isochron relationships, which support a virtually concurrent Archaean origin of garnet-free dunite (Re–Os T_{RD} & T_{MA} 2.6–3.1 Ga, Sm–Nd T_{CHUR} 2.9–3.3 Ga; Beyer *et al.*, 2004; Spengler, 2006) and enclosed pyroxenite (Sm–Nd 3.3 ± 0.2 Ga; Spengler *et al.*, 2009). In consequence, mantle garnet with lamellar pyroxene and Ti-oxide exsolution microstructures enclosed in cogenetic, extremely melt depleted peridotite points to a T above those of Archaean ambient upper mantle (Drury *et al.*, 2001; Spengler *et al.*, 2018; Spengler & Alifirova, 2019). Thus, it is likely that the portion of the central E Greenland SCLM represented by the exposed ultramafic bodies was part of a mantle plume.

Prograde metamorphism starting from UHP

Very low Al_2O_3 contents of 0.18–0.23 wt.% detected in cores of M3 orthopyroxene from Almklovdalen and Nogvadalen demonstrate that the dynamic recrystallisation in these two bodies occurred with increasing P (Figure 13). This P increase has lowered the Al_2O_3 content in rims of M2 orthopyroxene from Almklovdalen and Kalskaret resulting in the observed compositional zoning (Figure 9a, c). The cause of this prograde zoning is diffusion (i.e. not growth), because it characterises M2 orthopyroxene in porphyroclastic and granoblastic textures equally. Subsequent exhumation of the peridotite bodies overprinted M2 and M3 orthopyroxene leading to increasing Al_2O_3 contents at the crystal rims in all samples independent on texture and thus again by diffusion. The effectiveness of this Al diffusional overprint varies in orthopyroxene in the sample suite between ∼100 μm in the Almklovdalen and Kalskaret samples and ∼500 μm in the Gurskebotn and Raubergvik samples (Figures 9 and 10). Consequently, if the diffusion length has increased after burial, the original diffusion profile would be erased. Corresponding M2 orthopyroxene should form U-shaped Al_2O_3 concentration profiles. On the other hand, M2 orthopyroxene with low diffusion lengths obtained during exhumation should have preserved the preceding burial-related diffusion profile. Thus, a W-shaped Al_2O_3 profile should result from and indicate a prograde metamorphism. Because M2 grains with U-shaped and W-shaped Al_2O_3 profiles show long and short diffusion lengths, respectively (Figure 9), it is very likely that both groups of samples shared a prograde metamorphic evolution. Otherwise, the coincidence of U-shaped Al_2O_3 profiles and long diffusion lengths would be by chance.

The M3 grain size is of relevance when the chemical composition is used to infer the UHP metamorphic history. The recrystallised grains in the studied samples are usually small (few 100 μm). Thus, short Al diffusion lengths are required for preservation of the peak UHP metamorphic record. Correspondingly, the thermobarometric estimates are ambiguous: the M3 grains record P's for a given T that are either higher or lower than those derived from the M2 grains (Figure 13). The higher, diamond-field estimates characterise samples with low Al diffusion lengths and larger grain sizes (Almklovdalen, Nogvadalen), whereas the lower, sub-UHP estimates relate to samples with either long Aldiffusion length in orthopyroxene (Gurskebotn, Raubergvik) or very small grain size (Kalskaret). Therefore, we regard P estimates higher than those derived from the M2 grains to represent a minimum estimate for the peak metamorphic conditions and the latter as part of the retrograde evolution.

Another factor that influences the interpretation of iteratively calculated P–T estimates relates to the diffusion of elements used to determine T, i.e. Ca, Mg and Fe. Their diffusivity in pyroxene is faster than that of Al used to estimate P. This implies for small M3 grains with retrograde Al diffusion profiles (Figure 10) that any T estimate from these grains likely relates to post-peak P conditions. Fortunately, the M2 orthopyroxene porphyroclasts may constrain the evolution of T during tectonism in a similar fashion as they do for P. Irrespective of their strong Al zoning, the chemical gradients for Ca and Fe in M2 orthopyroxene are remarkably flat, except for some variation at the outermost grain rims (Figure 9). When combined with the element diffusivity then the flat Ca profiles could suggest that diffusion efficiently erased previous Ca concentrations in the M2 grains at some stage during the tectonic evolution. In this case, the coincidence of M2 P estimates (that are interdependent on T) in both average value and frequency distribution with those from comparable global SCLM xenoliths (that contain similar exsolution microstructures in garnet but lack a tectonic overprint) would be by chance (Figure 12). Furthermore, efficient Ca diffusion at 710 °C and 840 °C expects the M2 orthopyroxene Ca content to have undergone considerable modification during the subsequent retrograde T evolution, for which flat Ca profiles do not provide evidence. An alternative is that diffusion of Ca during tectonism was unable to significantly modify M2 grain cores. This would be the case if subduction and initial exhumation of the mantle rocks subparalleled Ca isopleths in orthopyroxene (Figure 13). Thermobarometry on different types of local crustal rocks (metapelite, gneiss, orthopyroxene-bearing eclogite and garnet-websterite) independently support an isopleth-subparallel metamorphic evolution

for crustal and mantle rocks in the Stadlandet–Nordfjord and Gurskøy–Storfjord areas (Figures 1 and 13).

Only samples from two orogenic peridotite bodies show recrystallised pyroxene that formed in the diamond stability field: Almklovdalen and Nogvadalen. The scatter of their M3 *P* estimates, ~1.5 GPa for each of the two bodies, is larger than that for any other body, <1.0 GPa (Figure 11a, b). Therefore, their *P–T* values appear less reliable for the determination of peak metamorphic conditions. However, the variably small M3 grain size combined with the relatively high and low diffusivity of elements used to estimate *T* (Ca, Mg, Fe) and *P* (Al), respectively, implies that the higher *P–T* values should more likely be nearer to the former peak metamorphic conditions than the lower values. In fact, the highest *P–T* estimate from Nogvadalen (6.2 GPa and 870 °C; Table 3) is indistinguishable from that of another sample with large M3 grain size (>1 mm) from the same locality (6.2 GPa and 877 °C; Spengler *et al.*, 2009). A conservative estimate for the peak conditions that affected the Almklovdalen samples can be obtained from the intersection of isopleths for Al in M3 orthopyroxene with those of Ca in M2 orthopyroxene, approximately 4.7 GPa and 770 °C (Figure 13). The highest *P–T* estimate from an Almklovdalen M3 average composition suggests some higher values of 5.4 GPa and 780 °C for the metamorphic peak (Table 3). These values overlap within uncertainty also the Ca isopleths from Almklovdalen M2 orthopyroxene (Figure 13). Thus, grain size, element diffusivity and thermobarometry on M2 and M3 grains collectively imply that the Almklovdalen body (exposed in the Stadlandet–Nordfjord area) was temporarily buried to a depth of approximately 150–170 km and that from Nogvadalen (Moldefjord area) to approximately 190 km as suggested earlier.

Samples from the other four bodies exposed in between (Gurskøy–Storfjord area) yielded average *P* values of only 2.3 GPa at 770 °C and 2.4 GPa at 730 °C depending on the use of either ortho- or clinopyroxene. These average *P–T* pairs for retrograde metamorphism of the studied mantle fragments overlap within uncertainty the isopleths for Ca in M2 orthopyroxene in these samples (Figure 13). Their tectonic burial depth is virtually unconstrained by the M3 data. However, the chemical equilibration of the M2 grain cores implies a minimum tectonic exhumation of 120 km for the four bodies.

Tectonic significance

Thermobarometry demonstrates that five of the six gneiss-hosted peridotite bodies equilibrated in the coesite stability field, while they resided in the mantle wedge (M2 in Figures 11 and 13). Application of these *P–T* data to the model of Brueckner (1998) for the incorporation of SCLM fragments into gneiss directly implies that the embedding crustal rocks have been at UHP metamorphic conditions. Other peridotite bodies were also shown to have equilibrated in the coesite field prior to recrystallisation (Figure 12). These include: Bardane (2.8 GPa, 733 °C; Spengler *et al.*, 2009), Kvalvika (NW Flemsøy; 3.5 GPa, 765 °C; Terry *et al.*, 2005), Raudhaugene (3.6 GPa, 762 °C; Medaris, 1984), Rødskar (E of Gurskebotn, 4.3 GPa, 859 °C; Medaris, 1984), Sandvik (W of Gurskebotn; 3.5 GPa, 855 °C; Medaris, 1984) and Ugelvik (3.6 GPa, 760 °C; Spengler *et al.*, 2009). If these eleven bodies constitute a representative suite, then all WGR Mg–Cr garnet-peridotites are likely derived from the coesite stability field. In this case they should all become included in UHP metamorphic areas. The consequence is a formidable expansion of the known UHP areas between Storfjord and Nordfjord, which may form a single area (Figure 1).

Areas defined by UHP eclogite contain garnet-peridotite bodies that show a favourable ratio between grain size and diffusion length in recrystallised M3 orthopyroxene required to preserve UHP conditions, e.g. Almklovdalen, Midsundvatnet, Nogvadalen, Raudhaugene and Ugelvik (this study; Spengler *et al.*, 2009, 2019). This prerequisite is absent in the studied bodies located in between these areas. For example, the Kalskaret M2 orthopyroxene with a W-shaped Al_2O_3 profile (Figure 9a) points to a prograde metamorphism beginning at conditions of the graphite–diamond phase transition (Figure 13). But M3 orthopyroxene of this sample is too small (120 μm, Supplementary Data Electronic Appendix 5) to preserve any UHP record in the mineral chemistry during retrogression (Figure 13). These differences in the efficiency of retrograde diffusion—demonstrated here for mantle samples with different diffusion lengths in and grain sizes of orthopyroxene—may also apply to adjacent cofacial gneiss and eclogite. Otherwise, (1) the occurrence of UHP-equilibrated peridotite bodies in between known UHP areas is difficult to explain and (2) the spatial correlation between ultramafics preserving prograde metamorphism and known UHP areas would be by chance. It follows that the metamorphic *P* gradients recorded in WGR crustal units may result from a superimposition of the true metamorphic conditions related to the subduction geometry and spatially variable rates of retrogression caused perhaps by inhomogeneous fluid activity. Thus, the M2 mantle minerals constrain the embedding crustal units to have been once at UHP metamorphic conditions regardless of whether they subsequently preserved or lost this record and whether crustal exhumation occurred as coherent slices or by ductile channel flow. This knowledge is essential for the reconstruction of ancient continent–continent collision zones.

The depth from which the mantle fragments were 'picked up' from the hangingwall determines the minimum lithostatic conditions their transport medium (gneiss) and its cargo (eclogite, peridotite) was exposed to. This simple causality implies for the WGR that Baltica crust was exposed to lithostatic *P* of the graphite–diamond phase transition (Figure 13).

Another inference can be drawn from the bodies' spatial distribution assuming that they share coherent Baltica plate segments (Young, 2018). The former residence depth of the ultramafics combined with the subduction geometry implies that the coastal Almklovdalen body became incorporated from ~100 km depth (3.0 GPa) into subducting Baltica gneiss at a time when the hinterland Kalskaret and Raubergvik bodies still resided in the mantle wedge. Continued Baltica plate subduction towards NW explains very low Al_2O_3 concentrations in Almklovdalen orthopyroxene, while the Kalskaret body (and Raubergvik body) became incorporated from ~120 km depth (3.7 GPa). An assumed subduction angle of 45° translates the subduction vector parallel distance between Almklovdalen and Kalskaret of ~60 km to a vertical distance of ~40 km (the vertical distance between Almklovdalen and Raubergvik would be ~30 km). This vertical distance corresponds to 1.4 GPa (or 1.0 GPa respectively) difference in lithostatic *P*. Thus, when the Kalskaret and Raubergvik bodies were incorporated from the SCLM, the Almklovdalen body was subducted already to ~160 km (or ~150 km) depth, i.e. to 5.1 GPa (or 4.7 GPa) of lithostatic *P*. This metamorphic *P* estimate exceeds the average *P* preserved in Almklovdalen M3 orthopyroxene (4.2 GPa), but agrees with the inferred peak metamorphic *P* conditions (4.7 GPa; Figure 13) and the highest *P* estimate from Almklovdalen (5.4 GPa; Table 3) given that W-shaped Al_2O_3 profiles in Kalskaret M2 orthopyroxene (Figure 9a) indicate a sustained subduction after the body's incorporation into gneiss. In other words, the diamond-grade M3 UHP metamorphic *P* estimates in the mantle fragments are consistent with lithostatic *P*. The maximum *P* estimate from Almklovdalen implies that subduction of the Kalskaret body continued for at least 10 vertical kilometres (0.3 GPa), i.e. to a depth of ~130 km (4.0 GPa).

Alternatively, if ductile extrusion in a subduction channel applies, then the spatial distribution of the ultramafics unlikely provides meaningful constraints on their metamorphic history. In this case, the similarity of *P* estimates deduced from M2 and M3 grains and subduction vector parallel distance of bodies described above would be by chance. Subduction channels have been proposed to be appropriate for the conceptual model of tectonic overpressure (Vrijmoed *et al.*, 2009). This concept interprets maximum *P* values to consist of lithostatic and non-lithostatic components, which queries M3 metamorphic estimates to represent burial depths (Cutts *et al.*, 2020). If relevant then non-lithostatic *P* components accompanied the formation of minerals with diamond-grade *P* estimates during tectonism in different rock types, i.e. gneiss (Dobrzhinetskaya *et al.*, 1995), crustal eclogite (Cuthbert *et al.*, 2000; Carswell *et al.*, 2006; Smith & Godard, 2013; Quas-Cohen, 2014), crustal pyroxenite (Vrijmoed *et al.*, 2006; Quas-Cohen, 2014) and mantle pyroxenite (van Roermund *et al.*, 2002; Carswell *et al.*, 2006; Spengler *et al.*, 2009, 2019, this study). Their exposure typifies the coastal sections of the three large UHP metamorphic areas (shaded in green in Figure 1). However, thermomechanical numerical simulations of subduction channels have shown that the proportion of tectonic overpressure at the plate interface is close to zero or even negative once the subducting continental crust reached the depth of the diamond stability field (Li *et al.*, 2010; Reuber *et al.*, 2016). Thus, these models support that all the diamond-grade metamorphic estimates in the different rock types represent lithostatic *P*. In addition, the depth of origin of several garnet-peridotite bodies in the SCLM hangingwall prior to tectonism (M2; Figure 12) independently demonstrates that mantle and embedding crustal rocks in coastal areas but also areas far from the coast and outside of known UHP areas (i.e. Kalskaret, Raubergvik) were at lithostatic conditions of the graphite–diamond phase transition. Therefore, a possible significant proportion of tectonic overpressure in the metamorphic record of the WGR garnet-peridotite bodies and surrounding rocks seems to be unlikely.

CONCLUSIONS

The study of ten SCLM samples in the WGR leads to the following conclusions:

1. To the authors' knowledge, we report the first bimineralic eclogite that contains garnet with acicular to subprismatic inclusions of pyroxene (omphacite) and rutile. These inclusions were inferred to have formed by exsolution from majoritic and titaniferous components.
2. Microstructural systematic variation of pyroxene and Ti-oxide inclusions with uniform distribution in garnet suggests up to four consecutive generations of solid-state exsolution. This primary microstucture was exposed to impregnating fluids and partial destruction by deformation and alteration.
3. A melt-related crystallisation of the majoritic and titaniferous precursor garnets requires mantle melting at $P > 3.7$ GPa and $T > 1600$ °C as expected for a plume environment. A lower *P* origin would preclude a majoritic garnet chemistry. An origin at lower *T* would demand a higher crystallisation *P* supported neither by the samples' equilibration depths in the SCLM, corresponding to 3.0–3.7 GPa, nor the physical process that stipulated the acicular exsolution, i.e. near isobaric cooling.
4. The samples' pre-tectonic equilibration at UHP in the SCLM hangingwall provides for different exhumation models a minimum exhumation depth for Baltica gneiss from lithostatic *P* equivalent to the graphite–diamond phase transition.
5. W-shaped Al_2O_3 concentration profiles in porphyroclastic orthopyroxene from coastal and hinterland samples indicate a prograde metamorphic evolution deep into the diamond stability field, which is confirmed by thermobarometry on recrystallised grains.

6. Areas that include UHP metamorphic rocks in the WGR are much larger than those mapped on the basis of eclogite occurrences. Presumably all garnet-peridotite bodies exposed in the WGR have experienced tectonic UHP metamorphism.

ACKNOWLEDGEMENTS

The authors wish to thank Marte Tøgersen and Roar Sandøy (Sibelco Nordic AS) for providing access to the Raubergvik mine, Franziska Scheffler (Jena University) for assistance in the field and Potsdam University students, most notably Lisa Dieck, Hannes Schildhauer and Pablo Kaiser, for their contribution with petrographical and petrological pilot studies within their training on individual samples. We would like to thank Thomas Theye for assistance at the EMP and Hans-Joachim Massonne for support of the study and favourable and critical comments, which led to substantial improvements in the manuscript. The manuscript benefited from the editorial handling by Jörg Hermann and from constructive reviews by himself and two anonymous reviewers.

FUNDING

This work was supported by the Russian Foundation for Basic Research grant No. 18–35–20072 to T.A.A., but did not receive any specific grant from funding agencies in the public, commercial, or not-for-profit sectors to the other authors.

SUPPLEMENTARY DATA

Supplementary data for this paper are available at Journal of Petrology online.

REFERENCES

Ackerson, M. R., Tailby, N. D. & Watson, E. B. (2017a). XAFS spectroscopic study of Ti coordination in garnet. *American Mineralogist* **102**, 173–183.

Ackerson, M. R., Watson, E. B., Tailby, N. D. & Spear, F. S. (2017b). Experimental investigation into the substitution mechanisms and solubility of Ti in garnet. *American Mineralogist* **102**, 158–172.

Ague, J. J. & Eckert, J. O. Jr. (2012). Precipitation of rutile and ilmenite needles in garnet: implications for extreme metamorphic conditions in the Acadian Orogen, U.S. *American Mineralogist* **97**, 840–855.

Anderson, D. L. (1989). *Theory of the Earth*. Blackwell Scientific Publications, Oxford.

Apeiranthiti, D. (2016). *An Investigation of the Metamorphic Evolution of the Kvalvika Garnet Peridotite Body, Flemsøya, Nordøyane, WGR, SW Norway*. M.Sc. thesis, Utrecht University. https://dspace.library.uu.nl/handle/1874/346410

Beyer, C., Frost, D. J. & Miyajima, N. (2015). Experimental calibration of a garnet–clinopyroxene geobarometer for mantle eclogites. *Contributions to Mineralogy and Petrology* **169**, 18.

Beyer, E. E., Brueckner, H. K., Griffin, W. L. & O'Reilly, S. Y. (2012). Laurentian provenance of Archean mantle fragments in the Proterozoic Baltic crust of the Norwegian Caledonides. *Journal of Petrology* **53**, 1357–1383.

Beyer, E. E., Brueckner, H. K., Griffin, W. L., O'Reilly, S. Y. & Graham, S. (2004). Archean mantle fragments in Proterozoic crust, Western Gneiss Region, Norway. *Geology* **32**, 609–612.

Bishop, F. C., Smith, J. V. & Dawson, J. B. (1976). Na, P, Ti and coordination of Si in garnet from peridotite and eclogite xenoliths. *Nature* **260**, 696–697.

Bizzarro, M. & Stevenson, R. K. (2003). Major element composition of the lithospheric mantle under the North Atlantic craton: evidence from peridotite xenoliths of the Sarfartoq area, southwestern Greenland. *Contributions to Mineralogy and Petrology* **146**, 223–240.

Brey, G. P. & Köhler, T. (1990). Geothermobarometry in four-phase lherzolites II. New thermobarometers, and practical assessment of existing thermobarometers. *Journal of Petrology* **31**, 1353–1378.

Brueckner, H. K. (1998). Sinking intrusion model for the emplacement of garnet-bearing peridotites into continent collision orogens. *Geology* **26**, 631–634.

Brueckner, H. K. (2018). The great eclogite debate of the Western Gneiss Region, Norwegian Caledonides: the in situ crustal v. exotic mantle origin controversy. *Journal of Metamorphic Geology* **36**, 517–527.

Brueckner, H. K., Carswell, D. A. & Griffin, W. L. (2002). Paleozoic diamonds within a Precambrian peridotite lens in UHP gneisses of the Norwegian Caledonides. *Earth and Planetary Science Letters* **203**, 805–816.

Brueckner, H. K., Medaris, L. G. Jr., Griffin, W. L., Johnston, S. M., Hartz, E. H., Pearson, N., Cai, Y. & Andresen, A. (2018). Mechanical mixing of garnet peridotite and pyroxenite in the orogenic peridotite lenses of the Tvaerdal Complex, Liverpool Land, Greenland Caledonides. *Journal of Petrology* **59**, 2191–2220.

Carswell, D. A. (1973). Garnet pyroxenite lens within Ugelvik layered garnet peridotite. *Earth and Planetary Science Letters* **20**, 347–352.

Carswell, D. A. (1986). The metamorphic evolution of Mg-Cr type Norwegian garnet peridotites. *Lithos* **19**, 279–297.

Carswell, D. A. & Cuthbert, S. J. (2003). "*Ultrahigh Pressure Metamorphism in the Western Gneiss Region of Norway*," In: Carswell, D. A. & Compagnoni, R. (eds.) *Ultrahigh Pressure Metamorphism*. Eötvös University Press, 51–73.

Carswell, D. A., Harvey, M. A. & Al-Samman, A. (1983). The petrogenesis of contrasting Fe-Ti and Mg-Cr garnet peridotite types in the high grade gneiss complex of Western Norway. *Bulletin de Minéralogie* **106**, 727–750.

Carswell, D. A. & van Roermund, H. L. M. (2005). On multi-phase mineral inclusions associated with microdiamond formation in mantle-derived peridotite lens at Bardane on Fjørtoft, west Norway. *European Journal of Mineralogy* **17**, 31–42.

Carswell, D. A., van Roermund, H. L. M. & Wiggers de Vries, D. F. (2006). Scandian ultrahigh-pressure metamorphism of Proterozoic basement rocks on Fjørtoft and Otrøy, Western Gneiss Region. *International Geology Review* **48**, 957–977.

Cherniak, D. J. & Dimanov, A. (2010). Diffusion in pyroxene, mica and amphibole. *Reviews in Mineralogy and Geochemistry* **72**, 641–690.

Cocks, L. R. M. & Torsvik, T. H. (2005). Baltica from the late Precambrian to mid-Palaeozoic times: the gain and loss of a terrane's identity. *Earth-Science Reviews* **72**, 39–66.

Collerson, K. D., Williams, Q., Kamber, B. S., Omori, S., Arai, H. & Ohtani, E. (2010). Majoritic garnet: a new approach to pressure estimation of shock events in meteorites and the encapsulation of sub-lithospheric inclusions in diamond. *Geochimica et Cosmochimica Acta* **74**, 5939–5957.

Corfu, F., Andersen, T. B. & Gasser, D. (2014). *"The Scandinavian Caledonides: main Features, Conceptual Advances and Critical Questions,"* In: Corfu, F., Gasser, D. & Chew, D. M. (eds.) *New Perspectives on the Caledonides of Scandinavia and Related Areas*. Geological Society, London, Special Publications, **390**, 9–43.

Cuthbert, S. & van Roermund, H. (2010). New evidence for majoritic garnet in central-belt orogenic peridotites of the Western Gneiss Complex, Norwegian Caledonides. *Geophysical Research Abstracts* **12**, EGU2010–14460.

Cuthbert, S. J., Carswell, D. A., Krogh-Ravna, E. J. & Wain, A. (2000). Eclogites and eclogites in the Western Gneiss Region, Norwegian Caledonides. *Lithos* **52**, 165–195.

Cutts, J. A., Smit, M. A., Spengler, D., Kooijman, E. & van Roermund, H. L. M. (2019). Two billion years of mantle evolution in sync with global tectonic cycles. *Earth and Planetary Science Letters* **528**, 115820.

Cutts, J. A., Smit, M. A. & Vrijmoed, J. C. (2020). Evidence for nonlithostatic pressure in subducted continental crust. *Contributions to Mineralogy and Petrology* **175**, 3.

Day, H. W. (2012). A revised diamond-graphite transition curve. *American Mineralogist* **97**, 52–62.

Dobrzhinetskaya, L. F., Eide, E. A., Larsen, R. B., Sturt, B. A., Trønnes, R. G., Smith, D. C., Taylor, W. R. & Posukhova, T. V. (1995). Microdiamond in high-grade metamorphic rocks from the Western Gneiss region. *Geology* **23**, 597–600.

Dowty, E. (1971). Crystal chemistry of titanian and zirconian garnet: I. Review and spectral studies. *American Mineralogist* **56**, 1983–2009.

Drury, M. R., van Roermund, H. L. M., Carswell, D. A., de Smet, J. H., van den Berg, A. P. & Vlaar, N. J. (2001). Emplacement of deep upper-mantle rocks into cratonic lithosphere by convection and diapiric upwelling. *Journal of Petrology* **42**, 131–140.

Fei, Y., Bertka, C. M. (1999). "*Phase Transitions in the Earth's Mantle and Mantle Mineralogy*," In: Fei, Y., Bertka, C. M. & Mysen, B. O. (eds.) *Mantle Petrology: Field Observations and High-Pressure Experimentation: A Tribute to Francis R. (Joe) Boyd, Special Publication No. 6*. "The Geochemical Society," Houston, 189–207.

Ganguly, J., Cheng, W. & O'Neill, H. S. C. (1993). Syntheses, volume, and structural changes of garnets in the pyrope-grossular join: implications for stability and mixing properties. *American Mineralogist* **78**, 583–593.

Ganne, J. & Feng, X. (2017). Primary magmas and mantle temperatures through time. *Geochemistry, Geophysics, Geosystems* **18**, 872–888.

Gasparik, T. (2000). An internally consistent thermodynamic model for the system CaO-MgO-Al_2O_3-SiO_2 derived primarily from phase equilibrium data. *The Journal of Geology* **108**, 103–119.

Gasparik, T. (2014). *Phase Diagrams for Geoscientists – an Atlas of the Earths Interior*. Springer, New York.

Gee, D. G., Janák, M., Majka, J., Robinson, P. & van Roermund, H. (2013). Subduction along and within the Baltoscandian margin during closing of the Iapetus Ocean and Baltica-Laurentia collision. *Lithosphere* **5**, 169–178.

Grew, E. S., Locock, A. J., Mills, S. J., Galuskina, I. O., Galuskin, E. V. & Halenius, U. (2013). Nomenclature of the garnet supergroup. *American Mineralogist* **98**, 785–811.

Griffin, W. L., Austrheim, H., Brastad, K., Bryhni, I., Krill, A. G., Krogh, E. J., Mørk, M. B. E., Qvale, H. & Tørudbakken, B. (1985). High-pressure metamorphism in the Scandinavian Caledonides. In: Gee, D. G. & Sturt, B. A. (eds.) The Caledonide Orogen–Scandinavia and Related Areas, Wiley, 783–801.

Griffin, W. L. & Brueckner, H. K. (1980). Caledonian Sm-Nd ages and a crustal origin for Norwegian eclogites. *Nature* **285**, 319–321.

Griffin, W. L. & Brueckner, H. K. (1985). REE, Rb-Sr and Sm-Nd studies of Norwegian eclogites. *Chemical Geology* **52**, 249–271.

Griffiths, T., Habler, G. & Abart, R. (2020). Determining the origin of inclusions in garnet: challenges and new diagnostic criteria. *American Journal of Science* **320**, 753–789.

Grütter, H. S., Gurney, J. J., Menzies, A. H. & Winter, F. (2004). An updated classification scheme for mantle-derived garnet, for use by diamond explorers. *Lithos* **77**, 841–857.

Gudfinnsson, G. H. & Presnall, D. C. (1996). Melting relations of model lherzolite in the system CaO-MgO-Al_2O_3-SiO_2 at 2.4–3.4 GPa and the generation of komatiites. *Journal of Geophysical Research: Solid Earth* **101**, 27701–27709.

Hacker, B. R., Andersen, T. B., Johnston, S., Kylander-Clark, A. R., Peterman, E. M., Walsh, E. O. & Young, D. (2010). High-temperature deformation during continental-margin subduction & exhumation: The ultrahigh-pressure Western Gneiss Region of Norway. Tectonophysics **480**, 149–171.

Hacker, B. R. (2006). Pressures and temperatures of ultrahigh--pressure metamorphism: implications for UHP tectonics and H_2O in subducting slabs. *International Geology Review* **48**, 1053–1066.

Hacker, B. R., Gerya, T. V. & Gilotti, J. A. (2013). Formation and exhumation of ultrahigh-pressure terranes. *Elements* **9**, 289–293.

Haggerty, S. E. & Sautter, V. (1990). Ultradeep (greater than 300 kilometers), ultramafic upper mantle xenoliths. *Science (New York, N.Y.)* **248**, 993–996.

Hasterok, D. & Chapman, D. S. (2011). Heat production and geotherms for the continental lithosphere. *Earth and Planetary Science Letters* **307**, 59–70.

Hawthorne, F. C., Oberti, R., Harlow, G. E., Maresch, W. V., Martin, R. F., Schumacher, J. C. & Welch, M. D. (2012). Nomenclature of the amphibole supergroup. *American Mineralogist* **97**, 2031–2048.

Henmi, C., Kusachi, I. & Henmi, K. (1995). Morimotoite, $Ca_3TiFe^{2+}Si_3O_{12}$, a New Titanian Garnet from Fuka, Okayama Prefecture, Japan. *Mineralogical Magazine* **59**, 115–120.

Herzberg, C., Condie, K. & Korenaga, J. (2010). Thermal history of the Earth and its petrological expression. *Earth and Planetary Science Letters* **292**, 79–88.

Hwang, S., Shen, P., Chu, H., Yui, T., Iizuka, Y. & Schertl, H. (2019). Rutile inclusions in garnet from a dissolution-reprecipitation mechanism. *Journal of Metamorphic Geology* **37**, 1079–1098.

Hwang, S. L., Shen, P., Chu, H. T., Yui, T. F. & Iizuka, Y. (2013). A TEM study of the oriented orthopyroxene and forsterite inclusions in garnet from Otry garnet peridotite, WGR,Norway: new insights on crystallographic characteristics and growth energetics of exsolved pyroxene in relict majoritic garnet. *Journal of Metamorphic Geology* **31**, 113–130.

Hwang, S.-L., Shen, P., Chu, H.-T., Yui, T.-F. & Iizuka, Y. (2015). Origin of rutile needles in star garnet and implications for interpretation of inclusion textures in ultrahigh-pressure metamorphic rocks. *Journal of Metamorphic Geology* **33**, 249–272.

Hwang, S. L., Yui, T. F., Chu, H., Shen, P., Schertl, H. P., Zhang, R. Y. & Liou, J. G. (2007). On the origin of oriented rutile needles in garnet from UHP eclogites. *Journal of Metamorphic Geology* **25**, 349–362.

Ito, J. & Frondel, C. (1967). Synthetic zirconium and titanium garnets. *American Mineralogist* **52**, 773–781.

Jamtveit, B. (1984). High-P metamorphism and deformation of the Gurskebotn garnet peridotite, Sunnmøre, western Norway. *Norsk Geologisk Tidsskrift* **64**, 97–110.

Jamtveit, B., Carswell, D. A. & Mearns, E. W. (1991). Chronology of the high-pressure metamorphism of Norwegian garnet peridotites/pyroxenites. *Journal of Metamorphic Geology* **9**, 125–139.

Jollands, M., Müntener, O. & Kaczmarek, M. A. (2016). Relative diffusivities of Cr, Al, Ti and Ca in natural orthopyroxene from the Lanzo massif (Italy) and their potential use in determininguplift rates. *AGU Fall Meeting, Abstract #V33D-3149*

Katayama, I., Karato, S-I. & Brandon, M. (2005). Evidence of high wate content in the deep upper mantle inferred from deformation microstructures. *Geology* **33**, 613–616.

Katayama, I., Parkinson, C. D., Okamoto, K., Nakajima, Y. & Maruyama, S. (2000). Supersilicic clinopyroxene and silica exsolution in UHPM eclogite and pelitic gneiss from the Kokchetav massif, Kazakhstan. *American Mineralogist* **85**, 1368–1374.

Katsura, T., Yoneda, A., Yamazaki, D., Yoshino, T. & Ito, E. (2010). Adiabatic temperature profile in the mantle. *Physics of the Earth and Planetary Interiors* **183**, 212–218.

Kawasaki, T. & Motoyoshi, Y. (2016). Ti-in-garnet thermometer for ultrahigh-temperature granulites. *Journal of Mineralogical and Petrological Sciences* **111**, 226–240.

Keller, D. S. & Ague, J. J. (2020). Quartz, mica, and amphibole exsolution from majoritic garnet reveals ultra-deep sediment subduction, Appalachian orogen. *Science Advances* **6**, eaay5178.

Klein, C. & Hurlbut, C. S. Jr. (1993). Manual of Mineralogy. *John Wiley & Sons* 681. pp.

Konzett, J., Frost, D. J., Proyer, A. & Ulmer, P. (2008). The Ca-Eskola component in eclogitic clinopyroxene as a function of pressure, temperature and bulk composition: an experimental study to 15 GPa with possible implications for the formation of oriented SiO_2-inclusions in omphacite. *Contributions to Mineralogy and Petrology* **155**, 215–228.

Krill, A. G. (1980). Tectonics of the Oppdal area, central Norway. *Geologiska Föreningen I Stockholm Förhandlingar* **102**, 523–530.

Krogh, E. J. (1977). Evidence of Precambrian continent–continent collision in Western Norway. Nature **267**, 17–19.

Kuang, Y., Xu, J., Li, B., Ye, Z., Huang, S., Chen, W., Zhang, D., Zhou, W. & Ma, M. (2019). Crystal-chemical properties of synthetic almandine-pyrope solid solution by X-ray single--crystal diffraction and Raman spectroscopy. *Crystals* **9**, 541.

Kullerud, L., Tørudbakken, B. O. & Ilebekk, S. (1986). A compilation of radiometric age determinations from the Western Gneiss Region, south Norway. *Norges Geologiske Undersøkelse Bulletin* **406**, 17–42.

Kylander-Clark, A. R. C. & Hacker, B. R. (2014). Age and significance of felsic dikes from the UHP western gneiss region. *Tectonics* **33**, 2342–2360.

Kylander-Clark, A. R. C., Hacker, B. R. & Cottle, J. M. (2013). Laser-ablation split-stream ICP petrochronology. *Chemical Geology* **345**, 99–112.

Kylander-Clark, A. R. C., Hacker, B. R., Johnson, C. M., Beard, B. L., Mahlen, N. J. & Lapen, T. J. (2007). Coupled Lu–Hf and Sm–Nd geochronology constrains prograde and exhumation histories of high- and ultrahigh-pressure eclogites from western Norway. *Chemical Geology* **242**, 137–154.

Lafuente, B., Downs, R. T., Yang, H. & Stone, N. (2015). "*The Power of Databases: The RRUFF Project*," In: Armbruster, T. & Danisi, R. M. (eds) *Highlights in Mineralogical Crystallography*. De Gruyter, 1–29.

Lapen, T. J., Medaris, L. G. Jr., Johnson, C. M. & Beard, B. L. (2005). Archean to Middle Proterozoic evolution of Baltica subcontinental lithosphere: evidence from combined Sm–Nd and Lu–Hf isotope analyses of the Sandvik ultramafic body. *Contributions to Mineralogy and Petrology* **150**, 131–145.

Lappin, M. A. (1973). An unusual clinopyroxene with complex lamellar intergrowths from an eclogite in the Sunndal-Grubse ultramafic mass. *Mineralogical Magazine* **39**, 313–320.

Li, Z. H., Gerya, T. V. & Burg, J.-P. (2010). Influence of tectonic overpressure on P–T paths of HP–UHP rocks in continental collision zones: thermomechanical modelling. *Journal of Metamorphic Geology* **28**, 227–247.

Liu, P. & Massonne, H.-J. (2019). An anticlockwise *P–T–t* path at high-pressure, high-temperature conditions for a migmatitic gneiss from the island of Fjørtoft, Western Gneiss Region, Norway, indicates two burial events during the Caledonian orogeny. *Journal of Metamorphic Geology* **37**, 567–588.

Locock, A., Luth, R. W., Cavel, R. G., Smith, D. G. W. & Duke, M. J. M. (1995). Spectroscopy of the cation distribution in the schorlomite species of garnet. *American Mineralogist* **80**, 27–38.

Ma, C. & Krot, A. N. (2014). Hutcheonite, $Ca_3Ti_2(SiAl_2)O_{12}$, a new garnet mineral from the Allende meteorite: an alteration phase in a Ca-Al-rich inclusion. *American Mineralogist* **99**, 667–670.

McDonald, C. S., Regis, D., Warren, C. J., Kelley, S. P. & Sherlock, S. C. (2018). Recycling argon through metamorphic reactions: the record in symplectites. *Lithos* **300–301**, 200–211.

McEnroe, S. A., Robinson, P., Langenhorst, F., Frandsen, C., Terry, M. P. & Ballaran, T. B. (2007). Magnetization of exsolution intergrowths of hematite and ilmenite: mineral chemistry, phase relations, and magnetic properties of hemo-ilmenite ores with micron- to nanometer-scale lamellae from Allard Lake, Quebec. *Journal of Geophysical Research* **112**, B10103.

Medaris, L. G. Jr. (1984). A geothermobarometric investigation of garnet peridotites in the Western Gneiss Region of Norway. *Contributions to Mineralogy and Petrology* **87**, 72–86.

Nakamura, D. (2009). A new formulation of garnet–clinopyroxene geothermometer based on accumulation and statistical analysis of a large experimental data set. *Journal of Metamorphic Geology* **27**, 495–508.

Nes, E. & Solberg, J. K. (1973). The dragging of precipitate particles by climbing dislocations in silicon. *Journal of Applied Physics* **44**, 488–489.

Paquin, J. (2001). Spurenelementverteilungen in Orogenen Granat-Peridotiten Und Granat-Olivin-Websteriten Als Indikator Ihrer Geochemischen Und Metamorphen Entwicklung Ph.D. thesis, Heidelberg University. https://d-nb.info/961897481/34

Povarennykh, A. S. & Shabalin, B. G. (1983). Structural role of titanium and iron in synthetic zirconium- and titanium-bearing garnets. *Geol Zhurnal* **43**, 45–50.in Russian)

Proyer, A., Habler, G., Abart, R., Wirth, R., Krenn, K. & Hoinkes, G. (2013). TiO_2 exsolution from garnet by open-system precipitation: evidence from crystallographic and shape preferred orientation of rutile inclusions. *Contributions to Mineralogy and Petrology* **166**, 211–234.

Quas-Cohen, A. (2014). *Norwegian Orthopyroxene Eclogites: petrogenesis and Implications for Metasomatism and Crust-Mantle Interactions during Subduction of Continental Crust PhD thesis*. University of Manchester. https://www.escholar.manchester.ac.uk/uk-ac-man-scw:239209

Reuber, G., Kaus, B. J., Schmalholz, S. M. & White, R. W. (2016). Nonlithostatic pressure during subduction and collision and the formation of (ultra)high-pressure rocks. *Geology* **44**, 343–346.

Reynes, J., Lanari, P. & Hermann, J. (2020). A mapping approach for the investigation of Ti–OH relationships in metamorphic garnet. *Contributions to Mineralogy and Petrology* **175**, 46.

Ringwood, A. E. (1967). The pyroxene-garnet transformation in the Earth's mantle. *Earth and Planetary Science Letters* **2**, 255–263.

Root, D. B., Hacker, B. R., Gans, P. B., Ducea, M. N., Eide, E. A. & Mosenfelder, J. L. (2005). Discrete ultrahigh-pressure domains in the Western Gneiss Region, Norway: implications for formation and exhumation. *Journal of Metamorphic Geology* **23**, 45–61.

Sand, K. K., Waight, T. E., Pearson, D. G., Nielsen, T. F. D., Makovicky, E. & Hutchison, M. T. (2009). The lithospheric mantle below southern West Greenland: a geothermobarometric approach to diamond potential and mantle stratigraphy. *Lithos* **112**, S, 1155–1166.

Sautter, V. & Fabriès, J. (1990). Cooling kinetics of garnet websterites from the Freychinède orogenic lherzolite massif, French Pyrenees. *Contributions to Mineralogy and Petrology* **105**, 533–549.

Sautter, V. & Harte, B. (1988). Diffusion gradients in an eclogite xenolith from the Roberts Victor kimberlite pipe: 1. mechanism and evolution of garnet exsolution in Al_2O_3-rich clinopyroxene. *Journal of Petrology* **29**, 1325–1352.

Scambelluri, M., Pettke, T. & van Roermund, H. L. M. (2008). Majoritic garnets monitor deep subduction fluid flow and mantle dynamics. *Geology* **36**, 59–62.

Schönig, J., Meinhold, G., von Eynatten, H. & Lünsdorf, N. K. (2018). Tracing ultrahigh-pressure metamorphism at the catchment scale. *Scientific Reports* **8**, 2931.

Schroeder-Frerkes, F., Woodland, A. B., Uenver-Thiele, L., Klimm, K. & Knapp, N. (2016). Ca-Eskola incorporation in clinopyroxene: limitations and petrological implications for eclogites and related rocks. *Contributions to Mineralogy and Petrology* **171**, 101.

Shannon, R. D. (1976). Revised effective ionic radii and systematic studies of interatomic distances in halides and chalcogenides. *Acta Crystallographica Section A* **32**, 751–767.

Smith, D. C. (1984). Coesite in clinopyroxene in the Caledonides and its implications for geodynamics. *Nature* **310**, 641–644.

Smith, D. C. (1988). "*A Review of the Peculiar Mineralogy of the 'Norwegian Coesite-Eclogite Province' with Crystal-Chemical, Petrological, Geochemical and Geodynamical Notes and an Extensive Bibliography*," In: Smith, D. C. (ed.) *Eclogites and Eclogite-Facies Rocks*. Elsevier, 1–206.

Smith, D. C. (2006). The SHAND quaternary system for evaluating the supersilicic or subsilicic crystal-chemistry of eclogite minerals, and potential new UHPM pyroxene and garnet end-members. *Mineralogy and Petrology* **88**, 87–122.

Smith, D. C. & Godard, G. (2013). A Raman spectroscopic study of diamond and disordered sp^3-carbon in the coesite-bearing Straumen Eclogite Pod. *Journal of Metamorphic Geology* **31**, 19–33.

Sobolev, A. V., Hofmann, A. W., Sobolev, S. V. & Nikogosian, I. K. (2005). An olivine-free mantle source of Hawaiian shield basalts. *Nature* **434**, 590–597.

Sobolev, N. V. & Lavrent'ev, J. G. (1971). Isomorphic sodium admixture in garnets formed at high pressures. *Contributions to Mineralogy and Petrology* **31**, 1–12.

Spencer, K. J., Hacker, B. R., Kylander-Clark, A. R. C., Andersen, T. B., Cottle, J. M., Stearns, M. A., Poletti, J. E. & Seward, G. G. E. (2013). Campaign-style titanite U–Pb dating by laser-ablation ICP: implications for crustal flow, phase transformations and titanite closure. *Chemical Geology* **341**, 84–101.

Spengler, D. (2006). Origin and evolution of deep upper mantle rocks from western Norway. *Ph.D. thesis, Faculteit Geowetenschappen, Universiteit Utrecht* https://dspace.library.uu.nl/handle/1874/13831.

Spengler, D. & Alifirova, T. A. (2019). Formation of Siberian cratonic mantle websterites from high-Mg magmas. *Lithos* **326–327**, 384–396.

Spengler, D., Brueckner, H. K., van Roermund, H. L. M., Drury, M. R. & Mason, P. R. D. (2009). Long-lived, cold burial of Baltica to 200 km depth. *Earth and Planetary Science Letters* **281**, 27–35.

Spengler, D., van Roermund, H. L. M. & Drury, M. R. (2018). Deep komatiite signature in cratonic mantle pyroxenite. *Journal of Metamorphic Geology* **36**, 591–602.

Spengler, D., van Roermund, H. L. M., Drury, M. R., Ottolini, L., Mason, P. R. D. & Davies, G. R. (2006). Deep origin and hot melting of an Archaean orogenic peridotite massif in Norway. *Nature* **440**, 913–917.

Spengler, D., van Roermund, H L M. & Scheffler, F. (2019). Pyroxene exsolution microstructures in garnet from the Almklovdalen peridotite. *SW Norway. Lithos* **350–351**, 105217.

Steinberger, B., Bredow, E., Lebedev, S., Schaeffer, A. & Torsvik, T. H. (2019). Widespread volcanism in the Greenland–North Atlantic region explained by the Iceland plume. *Nature Geoscience* **12**, 61–68.

St-Onge, M. R., van Gool, J. A. M., Garde, A. A. & Scott, D. J. (2009). Correlation of Archaean and Palaeoproterozoic units between northeastern Canada and western Greenland: constraining the pre-collisional upper plate accretionary history of the Trans-Hudson orogen. *Geological Society, London. Special Publications* **318**, 193–235.

Terry, M. P., Heidelbach, F., Couvy, H., Bromiley, G. D. & Krogh, T. (2005). PT history from the Kvalvika mantle peridotite, Norway: implications for crust-mantle interactions, and conditions and timing for olivine c-slip during continental subduction. *Geological Society of Amerika, Abstracts with Programs* **37**, 389.

Terry, M. P., Robinson, P., Carswell, D. A. & Gasparik, T. (1999). Evidence for a Proterozoic mantle plume and a thermotectonic model for exhumation of garnet peridotites, Western Gneiss Region, Norway. *EOS Transactions* **80**, S359–S360.

Tucker, R. D., Krogh, T. E. & Råheim, A. (1990). "Proterozoic Evolution and Age-Province Boundaries in the Central Part of the Western Gneiss Region, Norway: results of U-Pb Dating of Accessory Minerals from Trondheimsfjord to Geiranger," In: Gower, C. F., Ryan, B. & Rivers, T. (eds.): *Mid-Proterozoic Laurentia-Baltica, Geological Association of Canada, Special Paper*"," **38**, 149–173.

Tucker, R. D., Robinson, P., Solli, A., Gee, D. G., Thorsnes, T., Krogh, T. E., Nordgulen, Ø. & Bickford, M. E. (2004). Thrusting and extension in the Scandian hinterland, Norway: new U-Pb ages and tectonostratigraphic evidence. *American Journal of Science* **304**, 477–532.

van Roermund, H. L. M., Carswell, D. A., Drury, M. R. & Heijboer, T. C. (2002). Microdiamonds in a megacrystic garnet websterite pod from Bardane on the island of Fjørtoft, western Norway: evidence for diamond formation in mantle rocks during deep continental subduction. *Geology* **30**, 959–962.

van Roermund, H. L. M. & Drury, M. R. (1998). Ultra-high pressure ($P > 6$ GPa) garnet peridotites in western Norway: exhumation of mantle rocks from $>$ 185 km depth. *Terra Nova* **10**, 295–301.

van Roermund, H. L. M., Drury, M. R., Barnhoorn, A. & de Ronde, A. (2000a). Non-silicate inclusions in garnet from an ultra-deep orogenic peridotite. *Geological Journal* **35**, 209–229.

van Roermund, H. L. M., Drury, M. R., Barnhoorn, A. & de Ronde, A. (2000b). Super-silicic garnet microstructures from an orogenic garnet peridotite, evidence for an ultra-deep (>6 GPa) origin. *Journal of Metamorphic Geology* **18**, 135–147.

van Roermund, H. L. M., Drury, M. R., Barnhoorn, A. & de Ronde, A. (2001). Relict majoritic garnet microstructures from ultra-deep orogenic peridotites in western Norway. *Journal of Petrology* **42**, 117–130.

van Roermund, H., Spengler, D. & Vrijmoed, H. (2017). Micro-diamond in orogenic peridotite and other high grade metamorphics of the northern UHP domain, WGR, Norway: When and how did they form? *12th International Eclogite Conference in A˚re, Sweden – Post-conference excursion guide*. https://www.geology.lu.se/sites/geology.lu.se/files/iec12-_excursion-guide-vol-3.pdf

Vrijmoed, J. C., Podladchikov, Y. Y., Andersen, T. B. & Hartz, E. H. (2009). An alternative model for ultra-high pressure in the Svartberget Fe-Ti garnet-peridotite, Western Gneiss Region, Norway. *European Journal of Mineralogy* **21**, 1119–1133.

Vrijmoed, J. C., van Roermund, H. L. M. & Davies, G. R. (2006). Evidence for diamond-grade ultra-high pressure metamorphism and fluid interaction in the Svartberget Fe–Ti garnet peridotite–websterite body, Western Gneiss Region. *Mineralogy and Petrology* **88**, 381–405.

Wain, A. (1997). New evidence for coesite in eclogite and gneisses: defining an ultrahigh-pressure province in the Western Gneiss region of Norway. *Geology* **25**, 927–930.

Walczak, K., Cuthbert, S., Kooijman, E., Majka, J. & Smit, M. A. (2019). U–Pb zircon age dating of diamond-bearing gneiss from Fjørtoft reveals repeated burial of the Baltoscandian margin during the Caledonian Orogeny. *Geological Magazine* **156**, 1949–1964.

Walsh, E. O. & Hacker, B. R. (2004). The fate of subducted continental margins: two-stage exhumation of the high-pressure to ultrahigh-pressure Western Gneiss Region. *Journal of Metamorphic Geology* **22**, 671–687.

Warren, C. J., Beaumont, C. & Jamieson, R. A. (2008). Deep subduction and rapid exhumation: role of crustal strength and strain weakening in continental subduction and ultrahigh--pressure rock exhumation. *Tectonics* **27**, n/a.

Whitney, D. L. & Evans, B. W. (2010). Abbreviations for names of rock-forming minerals. *American Mineralogist* **95**, 185–187.

Yang, J. & Liu, L. (2004). Coupled isomorphic substitution and exsolution of pyroxene, rutile, apatite and quartz in supersilicic garnet. *Chinese Science Bulletin* **49**, 70–76.

Young, D. J. (2018). Structure of the (ultra)high-pressure Western Gneiss Region, Norway: imbrication during Caledonian continental margin subduction. *GSA Bulletin* **130**, 926–940.

Zhang, J. F., Xu, H. J., Liu, Q., Green, I. I. H. W. & Dobrzhinetskaya, L. F. (2011). Pyroxene exsolution topotaxy in majoritic garnet from 250 to 300 km depth. *Journal of Metamorphic Geology* **29**, 741–751.

Zhang, L., Song, S., Liou, J. G., Ai, Y. & Li, X. (2005). Relict coesite exsolution in omphacite from western Tianshan eclogites, China. *American Mineralogist* **90**, 181–186.